An accurate numerical solution to the Saint-Venant-Hirano model for mixed-sediment morphodynamics in rivers

Stecca, Guglielmo; Siviglia, Annunziato; Blom, Astrid

DOI
10.1016/j.advwatres.2015.05.022

Publication date
2016

Document Version
Accepted author manuscript

Published in
Advances in Water Resources

Citation (APA)
Stecca, G., Siviglia, A., & Blom, A. (2016). An accurate numerical solution to the Saint-Venant-Hirano model for mixed-sediment morphodynamics in rivers. *Advances in Water Resources*, *93*(Part A), 39-61. https://doi.org/10.1016/j.advwatres.2015.05.022

An accurate numerical solution to the Saint-Venant–Hirano model for mixed-sediment morphodynamics in rivers

Article *in* Advances in Water Resources · July 2016

DOI: 10.1016/j.advwatres.2015.05.022

3 authors:

Guglielmo Stecca
Università degli Studi di Trento
10 PUBLICATIONS **45** CITATIONS
SEE PROFILE

Annunziato Siviglia
ETH Zurich
47 PUBLICATIONS **494** CITATIONS
SEE PROFILE

Astrid Blom
Delft University of Technology
33 PUBLICATIONS **277** CITATIONS
SEE PROFILE

An accurate numerical solution to the Saint-Venant-Hirano model for mixed-sediment morphodynamics in rivers.

Guglielmo Stecca [a] Annunziato Siviglia [b] Astrid Blom [c]

[a] *National Institute of Water and Atmospheric Research (NIWA), Christchurch, New Zealand,*
and Department of Civil, Environmental and Mechanical Engineering, University of Trento, Trento, Italy.
Formerly: Faculty of Civil Engineering and Geosciences, Delft University of Technology, Delft, Netherlands.

[b] *Laboratory of Hydraulics, Hydrology and Glaciology VAW, ETH Zurich, Zurich, Switzerland.*

[c] *Faculty of Civil Engineering and Geosciences, Delft University of Technology, Delft, Netherlands.*

Abstract

We present an accurate numerical approximation to the Saint-Venant-Hirano model for mixed-sediment morphodynamics in one space dimension. Our solution procedure originates from the fully-unsteady matrix-vector formulation developed in [54]. The principal part of the problem is solved by an explicit Finite Volume upwind method of the path-conservative type, by which all the variables are updated simultaneously in a coupled fashion. The solution to the principal part is embedded into a splitting procedure for the treatment of frictional source terms. The numerical scheme is extended to second-order accuracy and includes a bookkeeping procedure for handling the evolution of size stratification in the substrate. We develop a concept of balancedness for the vertical mass flux between the substrate and active layer under bed degradation, which prevents the occurrence of non-physical oscillations in the grainsize distribution of the substrate. We suitably modify the numerical scheme to respect this principle. We finally verify the accuracy in our solution to the equations, and its ability to reproduce one-dimensional morphodynamics due to streamwise and vertical sorting, using three test cases. In detail, i) we empirically assess the balancedness of vertical mass fluxes under degradation; ii) we study the convergence to the analytical linearised solution for the propagation of infinitesimal-amplitude waves [54], which is here employed for the first time to assess a mixed-sediment model; iii) we reproduce Ribberink's E8-E9 flume experiment [46].

Key words: Non-conservative hyperbolic systems, Mixed sediment, Numerical

morphodynamics, Active layer, Sediment transport, Path-conservative method, Upwind methods

1 Introduction

The presence of mixed sediment is a prominent feature of the morphology of rivers and a key driver of their morphodynamic evolution at different scales [42]. The mathematical description of mixed-sediment morphodynamics is based on proper sediment continuity models, relating bedload transport to the size of sediment available at the bed surface, and keeping track of the development of size stratification within the bed. Hirano [26,27] was the first to develop such a model. He discretised the bed material using a finite number of classes, each characterized by a representative grain size, and put forward the concept of the active layer, i.e. a fully-mixed layer located just under the bed surface. In most applications, the active layer model is employed in conjunction with a flow model given by the Saint-Venant equations, and the resulting system of partial differential equation is referred to as the Saint-Venant-Hirano model, e.g. [54].

Despite the availability of more refined approaches to mixed-sediment morphodynamics, such as the two-layer model of Ribberink [46] and a vertical-continuous approach, e.g. [45,4,6], the active layer approach has remained the most popular strategy over the last four decades. It has been extensively applied both in analytical models, e.g. [44,46,16,47,33], and numerical models. In detail, numerical solutions to the Hirano equations have been used to study e.g., static bed armouring [1], sediment sorting induced by dunes [46], patterns of downstream fining [28,18], development of size stratification of the bed in rivers and deltas [63,62], pool-riffle dynamics [36], sediment pulses in mountain streams [20,19]. The active layer mode is also implemented in multi-purpose, mainstream morphodynamic software, e.g. Delft3D [51] and BASEMENT [61]. These modelling attempts have been accompanied by characteristic analyses of the system, conducted in increasingly-refined way in [46,49,54], where the propagation of morphodynamic changes as described by the system eigenstructure has been theoretically investigated.

Two aspects must be considered when a numerical model is developed. First, the mathematical model must properly describe all the relevant physical features, at least in simplified manner, through an appropriate system of gov-

Email addresses: Gu.Stecca@niwa.co.nz (Guglielmo Stecca), siviglia@vaw.baug.ethz.ch (Annunziato Siviglia), Astrid.Blom@tudelft.nl (Astrid Blom).

erning equations. In addition to this, the system must be solved accurately, since a poor numerical solution may considerably differ from the exact solution to the same system of equations, and thus be far from reproducing reliable physical results, even if the physics is correctly captured by the mathematical model. The request for accurate numerical solutions in mixed-sediment morphodynamics becomes even more important, if one considers that model results are themselves heavily dependent on the calibration of empirical submodels for friction, sediment transport and active layer thickness [38], and that the interaction between these inherent uncertainties and additional inaccuracies of numerical source shall be ideally avoided. Noticeably, increasing effort has been devoted to this aim in recent years, with the application of refined second-order Finite Volume techniques to mixed-sediment modelling, e.g. [29].

The aim of this paper is to develop and assess an accurate numerical solution procedure to the Saint-Venant-Hirano model, and to show that the improved numerical accuracy is effective in improving the morphodynamic prediction. The proposed solver adopts a synchronous solution strategy, whereby the equations are solved all together in a coupled fashion, by straightforwardly discretising the fully-unsteady matrix-vector (non-conservative) formulation developed in [54]. This has a number of advantages. First, the advection of hydrodynamic and morphodynamic changes is entirely determined by the eigenstructure of the matrix, and thus the numerical solution converges to the linearised solution for the propagation of multiple sorting waves [54]. Furthermore, the stability condition of the global hydro-morphodynamic scheme is explicitly known and given by the standard CFL condition, without the need of further reducing the time step for the stabilisation of morphodynamic computations, e.g., [31]. Finally, the knowledge of the coupled hydro-morphodynamic evolution of the system in time, given in our case by the matrix-vector formulation, allows for extension of the scheme to second-order accuracy in space and time for all the variables, which significantly reduces the effect of numerical dissipation.

The use of a non-conservative formulation mandates the adoption of the path-conservative framework [21,41], by which the weak solutions of the Finite Volume technique are still defined. To our knowledge, the path-conservative approach, which has become increasingly popular in unisize-sediment morphodynamics governed by the Saint-Venant-Exner model, e.g. [9,56,8,10,7,50], is here employed for the first time for modelling mixed-sediment morphodynamics. In detail we implement the DOT scheme of Dumbser and Toro [23]. This scheme combines the accuracy of an upwind scheme based on a complete Riemann solver with flexibility and generality, due to the fact that the Roe averages do not have to be explicitly known, unlike in classical Roe schemes, e.g. [9]. This is key in our case, since the complexity of the system matrix rapidly increases when more sediment fractions are considered. The numer-

ical scheme is extended to second-order accuracy in the ADER framework, e.g., [59], and the solution algorithm includes a mass-conservative procedure for the bookkeeping of size stratification and vertical sorting in the substrate, e.g., [63,62].

Furthermore, we introduce a concept of balancedness which applies to the modelling of mixed-sediment morphodynamics, and regards the vertical sediment mass flux from the substrate to the active layer under bed degradation. This principle prevents the discrete numerical scheme from modifying the grainsize distribution of the remaining substrate when the interface with the active layer drops and the upper portion of the substrate is mined, as prescribed by the active layer model in differential form. We point out that this is relevant also for existing codes based on the active layer approach, which include an administration procedure for size stratification in the substrate. Concerning our model, we suitably modify the DOT scheme to achieve the sought balance, and experimentally show that this is crucial for obtaining an accurate and robust description of the evolution of the vertical sorting profile.

We further assess the model with two test cases. One of them concerns the convergence to the analytical solution for the propagation of small-amplitude hydro-morphodynamic waves [54]. This is an innovative test case and one of the few, in mixed-sediment morphodynamics, having a benchmark analytical solution, and is thus ideal to purely assess the accuracy of the solver. Our solution based on the DOT method is found significantly more accurate than a competing solution based on the PRICE-C centred method [8] due to lower dissipation, and our second-order scheme is shown to converge to the analytical solution. The last test is about the modelling of the experimental setup of Ribberink [46] (run E8-E9), concerning morphodynamic adaptation to changes in sediment feed, in bedform-dominated conditions. The model well predicts the speed of streamwise sorting and morphodynamic changes, and the match with available laboratory data is improved with respect to previous modelling reproductions based on the active layer approach [3]. Moreover, our solution enables us to clearly identify the limitations of the underlying active layer schematisation, which are mainly related to over-simplification of vertical sediment fluxes, see [4].

2 The mathematical model

We consider unsteady free-surface shallow flow over a cohesionless bed, in one space dimension. Friction exerted by flow induces sediment transport, which occurs only as bedload. The bed is composed of mixed sediment, and the active layer approach of Hirano [26,27] is used to account for this feature. In a recent work [54], to which we refer the reader for detail, we have derived

and thoroughly analysed the model, by generalising the previous analyses in [46,49,39]. In this section we will briefly recall the underlying schematisation and the relevant equations.

2.1 Governing equations

The Saint-Venant-Hirano model [54] includes equations for the conservation of water mass (continuity equation)

$$\partial_t h + \partial_x q = 0 \ , \tag{1}$$

for the momentum principle applied to the water phase

$$\partial_t q + \partial_x \left(\frac{q^2}{h} + \frac{1}{2} g h^2 \right) + g h \partial_x \eta = -g h S_f \ , \tag{2}$$

and for the conservation of total sediment mass (the Exner equation):

$$\partial_t \eta + \partial_x q_b = 0 \ . \tag{3}$$

Equations (1)-(3) form the Saint-Venant-Exner model, e.g., [34,35] which governs one-dimensional morphodynamics when a single sediment fraction is considered (unisize-sediment case). Here, t $[s]$ is time, x $[m]$ is the streamwise coordinate, h $[m]$ is the flow depth, q $[m^2 s^{-1}]$ is the flow discharge per unit width, η $[m]$ is the bed elevation, $g = 9.8\ ms^{-2}$ is the acceleration due to gravity, q_b $[m^2 s^{-1}]$ is the total sediment discharge, which includes the effect of porosity, and S_f $[-]$ is the friction slope, to be specified by a closure relation in Section 2.2

The active layer approach [26,27] provides additional continuity equations for mixed sediment. The sediment mixture is discretised into N fractions, each one characterized by one representative grain diameter d_k, where k is an index in the range $[1, N]$. The sediment discharge of each size fraction q_{bk} is defined using appropriate closure relations, which will be described in Section 2.2. The total sediment discharge q_b in (3) is then given by

$$q_b = \sum_{k=1}^{N} q_{bk} \ . \tag{4}$$

We adopt a vertical discretisation of the bed into two layers, as shown in Fig. 1. The active layer is a moving sediment volume located just underneath the bed surface, and represents the sediment which interacts with flow, giving rise to sediment discharge. It is vertically mixed and has vertically-averaged grainsize distribution $F_{ak}(x,t)$ $[-]$. Following [46,54], we assume the active

layer thickness L_a to be constant in time, i.e.

$$\partial_t L_a = 0 \, . \tag{5}$$

Thus, the vertical displacement of this layer only varies with the bed elevation $\eta\,(x,t)$.

The substrate is located under the active layer. It is not vertically mixed and has grainsize distribution $f_{sk}(x,z,t)$. The interface between the two layers is located at elevation $z = \eta - L_a$ (see Fig. 1). The substrate is not directly affected by bedload discharge, and only exchanges mass with the active layer. The exchange of sediment between the two layers occurs only by net increase or decrease in the elevation of the interface at $z = \eta - L_a$, and this vertical mass flux is compensated by consumption or creation of new substrate on top of the layer.

Under the assumed time constancy of active layer thickness (5), the resulting sets of integral mass conservation per size fraction equations are

$$\partial_t M_{ak} + \partial_x q_{bk} - f_k^I \partial_x q_b = 0 \qquad \text{for } 1 \leq k \leq N-1 \, , \tag{6}$$

and

$$\partial_t M_{sk} + f_k^I \partial_x q_b = 0 \qquad \text{for } 1 \leq k \leq N-1 \, , \tag{7}$$

in the active layer and substrate, respectively. Here, f_k^I is the grainsize distribution at the interface between the active layer and the substrate, which, as in [26,27,46,3,54] is computed by

$$f_k^I = \begin{cases} F_{ak} & \text{if } \partial_t \left(\eta - L_a\right) > 0 \\ f_{sk}\left(z = \eta - L_a\right) & \text{if } \partial_t \left(\eta - L_a\right) < 0 \end{cases} \, , \tag{8}$$

in agreement with the vertical mass exchange mechanism described above. It is worth mentioning that alternative relations to (8), have been proposed in [43,28,60], whereby f_k^I in aggradational conditions is computed as a weighted average of the grainsize distribution of bedload and of that in the active layer F_{ak}. As the purpose of the present paper is not to test alternative closure relations for the interface fractions under aggradation, but to develop an accurate solution procedure to the model, we will not further consider these relations, and favour the original formulation by Hirano [26,27] in (8). However, there is no theoretical barrier to their implementation in the model in further work.

In (6) and (7), M_{ak} and M_{sk} $[m]$ represent the sediment mass of the kth fraction per surface area in the active and substrate layer, divided by the constant sediment density, in the active and substrate layer. These are given by

$$M_{ak} = F_{ak} L_a \, , \qquad M_{sk} = \int_{\eta_0}^{\eta - L_a} f_{sk}\left(z\right) \mathrm{d}z \, , \tag{9}$$

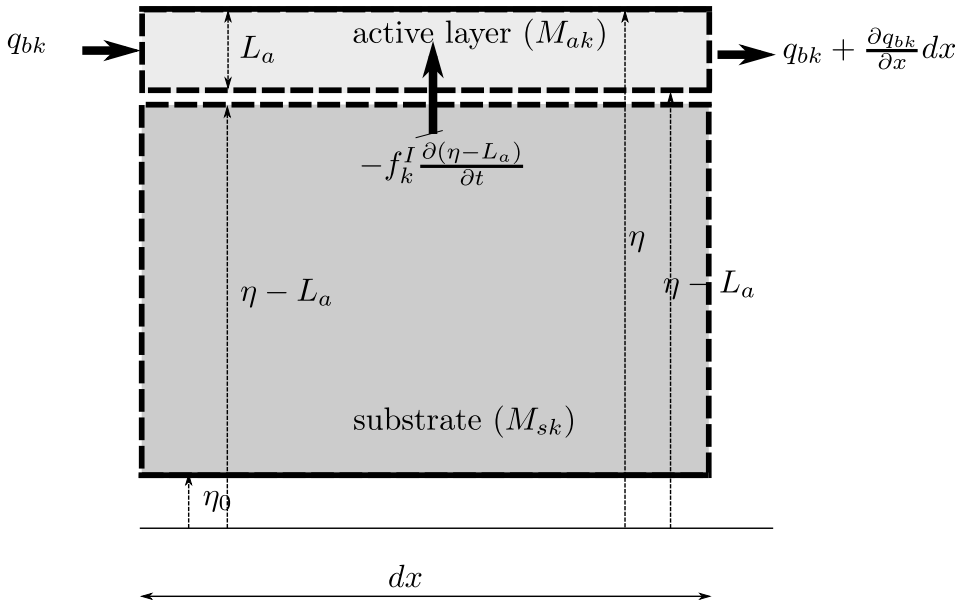

Fig. 1. Sketch and notation of the vertical discretisation of the river bed and sediment fluxes.

where η_0 is a time-constant reference elevation datum (see Fig. 1). The mass variables (9) are subject to the constraint

$$\sum_{k=1}^{N} M_{ak} = L_a \ , \qquad \sum_{k=1}^{N} M_{sk} = \eta - L_a - \eta_0 \ . \tag{10}$$

It follows from (10) that only $N-1$ independent active layer equations (6) and substrate equations (7) are required for describing the evolution of the grain-size distribution throughout the domain, since the mass of the Nth fraction is recovered as

$$M_{aN} = L_a - \sum_{k=1}^{N-1} M_{ak} \qquad , \qquad M_{sk} = \eta - L_a - \eta_0 - \sum_{k=1}^{N-1} M_{sk} \ , \tag{11}$$

where η is provided by the solution of the Exner equation (3). Therefore, when the problem is written for N size fractions, the system includes $2N+1$ partial differential equations (PDEs), namely the three equations of the Saint-Venant-Exner model (1)-(3), $N-1$ active layer equations (6) and $N-1$ substrate equations (7).

2.2 Closure relations

The friction slope S_f in the momentum equation (2) is evaluated by the Chèzy law as

$$S_f = \frac{q^2}{C^2 g h^3} \ , \tag{12}$$

where C is the dimensionless Chèzy coefficient, assumed as constant.

The sediment discharge q_{bk} of each fraction, to be used in (6), and, after computation of total sediment transport (4), in (3), (6) and (7) is computed as

$$q_{bk} = F_{ak} Q_{bk} = \frac{M_{ak}}{L_a} Q_{bk} \ , \tag{13}$$

where Q_{bk} is the transport capacity for the case that the bed would consist only of the size fraction, (yet, possibly including a hiding-exposure correction). For its evaluation we consider the relation of Meyer-Peter and Müller [37], which reads

$$Q_{bk} = \text{sign}\,(q)\, A \frac{\sqrt{g \Delta d_k^3}}{1-\epsilon} \max\left(\left(\theta_k - \xi_k \theta_c\right), 0\right)^B \ , \tag{14}$$

where ϵ (constant) is the bed porosity, A, B are dimensionless constant parameters, θ_c is the critical Shields stress, ξ_k is the hiding-exposure correction of critical Shields stress for the kth sediment fraction, and finally $\Delta = \rho_s/\rho - 1$, where $\rho_s = 2650\ kg\,m^{-3}$ and $\rho = 1000\ kg\,m^{-3}$ are sediment and water density. Furthermore, in (14) θ_k is the Shields number relative to the kth fraction, defined as

$$\theta_k = \mu \frac{S_f h}{\Delta d_{sk}} \ , \tag{15}$$

where S_f is given by (12), and $\mu \leq 1$ is the ripple factor, i.e., a reduction coefficient which takes into account the fact that, if the river bed is covered by bedforms, only the skin friction component of S_f, and not the bedform drag component, induces bedload transport [46].

Finally in (14) for the evaluation of the hiding factor we implement the formulation due to Egiazaroff [24], which reads

$$\xi_k = \left(\frac{\log_{10} 19}{\log_{10}\left(19 \frac{d_k}{\overline{d}}\right)} \right)^2 \ , \tag{16}$$

where $\overline{d} = \sum_{k=1}^{N} F_{ak} d_k$ is the mean sediment diameter in the active layer. Alternatively, we consider in our code the case without hiding correction, where we set $\xi_k = 1$ for all fractions.

2.3 The system in matrix-vector form

We first rewrite the system of governing equations in an equivalent form, which is most suitable for numerical discretisation, by using as conserved variable the free-surface elevation $H = h + \eta$ rather than the flow depth h, e.g. [50].

With this change of variables, the system of governing equations (1)-(2)-(3)-

(6)-(7) has matrix-vector (non-conservative) formulation

$$\partial_t \mathbf{Q} + \mathbf{A}\partial_x \mathbf{Q} = \mathbf{S}\ , \tag{17}$$

where the vector of unknowns $\mathbf{Q}$ is

$$\mathbf{Q} = \left[H,\ q,\ \eta,\ \underbrace{M_{a1},\ \ldots\ ,\ M_{aN-1}}_{N-1},\ \underbrace{M_{s1},\ \ldots\ ,M_{sN-1}}_{N-1} \right]^T\ , \tag{18}$$

the vector of source terms $\mathbf{S}$ is

$$\mathbf{S} = \left[0, -ghS_f,\ 0,\ \underbrace{0,\ \ldots\ ,\ 0}_{N-1},\ \underbrace{0,\ \ldots\ ,0}_{N-1} \right]^T\ . \tag{19}$$

and the system matrix is

$$\mathbf{A} = \left[\begin{array}{ccc|c|c} \frac{\partial q_b}{\partial H} & 1+\frac{\partial q_b}{\partial q} & \frac{\partial q_b}{\partial \eta} & \left[\frac{\partial q_b}{\partial M_{al}}\right] & [0] \\ gh-u^2 & 2u & u^2 & [0] & [0] \\ \frac{\partial q_b}{\partial H} & \frac{\partial q_b}{\partial q} & \frac{\partial q_b}{\partial \eta} & \left[\frac{\partial q_b}{\partial M_{al}}\right] & [0] \\ \hline \left[\frac{\partial q_{bk}}{\partial H} - f_k^I \frac{\partial q_b}{\partial H}\right] & \left[\frac{\partial q_{bk}}{\partial q} - f_k^I \frac{\partial q_b}{\partial q}\right] & \left[\frac{\partial q_{bk}}{\partial \eta} - f_k^I \frac{\partial q_b}{\partial \eta}\right] & \left[\frac{\partial q_{bk}}{\partial M_{al}} - f_k^I \frac{\partial q_b}{\partial M_{al}}\right] & [0] \\ \hline \underbrace{\left[f_k^I \frac{\partial q_b}{\partial H}\right]}_{1} & \underbrace{\left[f_k^I \frac{\partial q_b}{\partial q}\right]}_{1} & \underbrace{\left[f_k^I \frac{\partial q_b}{\partial \eta}\right]}_{1} & \underbrace{\left[f_k^I \frac{\partial q_b}{\partial M_{al}}\right]}_{N-1} & \underbrace{[0]}_{N-1} \end{array} \right] \begin{array}{l} \}1 \\ \}1 \\ \}1 \\ \}N-1 \\ \}N-1 \end{array}\ , \tag{20}$$

where $u = q/h\ [ms^{-1}]$ is the flow velocity and the integer indices k and l span the range $[1, N-1]$. The matrix has size $(2N+1) \times (2N+1)$ when the system is written for N fractions. The present formulation slightly differs from that in [54], due to the above change of variables (i.e., use of water elevation rather than flow depth as dependent variable) adopted in this paper, and because here the frictional source term in the momentum equation is retained. In spite of these differences, the eigenstructure analysis in [54] applies here entirely.

A key point in this respect is the study of the hyperbolicity domain in [54,46,49], by which the conditions under which the problem has real eigenvalues (hyperbolic behaviour) or complex eigenvalues (elliptic behaviour) were determined. Unlike the Saint-Venant-Exner model for unisize sediment, which was found to be safely hyperbolic for all the range of Froude number reasonably encountered in real streams [17], the Saint-Venant-Hirano model may switch to elliptic behaviour under relatively common and physically significant settings of data and parameters. In detail, whereas the problem is always hyperbolic under aggradational conditions, hyperbolicity may be lost in degradational cases, if the active layer is coarser than the substrate. Ellipticity represents a

severe shortcoming, since elliptic models in classical mechanics are conceptually inadequate for representing time-advancing problems [38] and initial-value elliptic problems are mathematically ill-posed, e.g., [30,58]. Therefore, numerical solutions of elliptic problems by time-advancing numerical schemes might display non-physical oscillations, as reported for this model in [13,14,46,49] or for other models in fluid mechanics, e.g. [11]. It is beyond the purpose of this paper to solve this issue, which is matter of current work by the authors. For the time being, all the numerical simulations in Section 4 have been conducted within the hyperbolic range.

3 Numerical solution

We aim at numerically solving the initial-value problem (IVP) given by the one-dimensional non-conservative hyperbolic system of PDEs (17)-(20) and appropriate initial conditions. We discretise the computational domain by n_c cells having the same size Δx. The initial data in the cell $\mathcal{C}_i$ at time t^n are represented by cell averages $\mathbf{Q}_i^n$ and the numerical solution sought at time $t^{n+1} = t^n + \Delta t$ is denoted with $\mathbf{Q}_i^{n+1}$. The full IVP reads

$$\left.\begin{array}{lll} \text{PDEs: } \partial_t \mathbf{Q} + \mathbf{A}\partial_x \mathbf{Q} = \mathbf{S} & & \\ \text{IC:} \quad \mathbf{Q}(x,0) & = \mathbf{Q}_i^n & \end{array}\right\} \overset{\Delta t}{\Longrightarrow} \mathbf{Q}_i^{n+1} \quad \text{IVP} \,. \tag{21}$$

The system (17) is non-homogeneous due to the presence of frictional source terms (19). This is handled adopting a robust splitting technique [57,53,50] which formally preserves second order accuracy. We will briefly introduce this procedure, while referring the reader to [50,53] for a full description.

The solution to the full IVP (21) is achieved by sequentially solving three IVPs. Within IVP1, the solution is updated by a time step $\frac{1}{2}\Delta t$, starting from the initial condition $\mathbf{Q}_i^n$, and only taking into account the system of ordinary differential equations (ODEs) which stems from the frictional source terms, i.e.,

$$\left.\begin{array}{lll} \text{ODEs: } \frac{\mathrm{d}\mathbf{Q}}{\mathrm{d}t} & = \mathbf{S} & \\ \text{IC:} \quad \mathbf{Q}(x,0) & = \mathbf{Q}_i^n & \end{array}\right\} \overset{\frac{1}{2}\Delta t}{\Longrightarrow} \overline{\mathbf{Q}}_i \quad \text{IVP1} \,. \tag{22}$$

Then, within IVP2 the solution is integrated by Δt, taking as initial condition the output of IVP1 (22) $\overline{\mathbf{Q}}_i$, by considering the homogeneous hyperbolic system which resembles the inviscid problem, i.e.,

$$\left.\begin{array}{ll} \text{PDEs: } \partial_t \mathbf{Q} + \mathbf{A}\partial_x \mathbf{Q} = \mathbf{0} \\ \text{IC:} \qquad \mathbf{Q}\left(x,0\right) \qquad\quad = \overline{\mathbf{Q}}_i \end{array}\right\} \overset{\Delta t}{\Longrightarrow} \overline{\overline{\mathbf{Q}}}_i \quad \text{IVP2} \; . \tag{23}$$

Finally, IVP3 is analogous to IVP1 (22), but has initial condition $\overline{\overline{\mathbf{Q}}}_i$, which corresponds to the solution of IVP2. The output of IVP3, denoted with $\mathbf{Q}_i^{n+1}$, represents the solution to the full IVP (21).

In the next sections, we will focus on the solution to the inviscid Saint-Venant-Hirano model in IVP2 (23), to be achieved in a synchronous manner for all variables by a second-order accurate Finite Volume technique. Since a conservation-law form for this system is not available, the non-conservative formulation (17) will be straightforwardly integrated, by application of path-conservative methods.

3.1 Solution to IVP2: the DOT path-conservative scheme

We consider the homogeneous non-conservative hyperbolic system of PDEs

$$\partial_t \mathbf{Q} + \mathbf{A}\partial_x \mathbf{Q} = \mathbf{0} \; . \tag{24}$$

with vector of variables $\mathbf{Q}$ (18) and matrix $\mathbf{A}$ (20). The initial condition at $t = t^n$ is denoted with $\overline{\mathbf{Q}}_i$, and the solution at $t = t^n + \Delta t$ with $\overline{\overline{\mathbf{Q}}}_i$.

Time integration is explicit. Therefore, the time step Δt is chosen small enough to comply with a standard CFL stability condition, having the form

$$\Delta t = \frac{CFL\,\Delta x}{\max_{1\leq i\leq n_c} |\lambda|_i^{max}} \tag{25}$$

with $CFL < 1$. Here, $|\lambda|_i^{max}$ is the maximum absolute eigenvalue of the system matrix computed with the initial data in cell $\mathcal{C}_i$, for which, following [54], we use the fixed-bed approximation $|\lambda|_i^{max} \approx |u| + \sqrt{gh}$ for efficient implementation. The CFL condition (25) guarantees the stability to the full hydro-morphodynamic solution, without the need for any further reduction of the time step for the stabilisation of morphodynamic computations, as done in asynchronous solutions, e.g.[31]. Furthermore, when frictional source terms are considered, it guarantees the stability in the solution to the full IVP (21), since IVP1 (22) and IVP3 are integrated by an unconditionally-stable, implicit Runge-Kutta scheme [50].

First-order path-conservative schemes [21,41] are given by the update formula

$$\overline{\overline{\mathbf{Q}}}_i = \overline{\mathbf{Q}}_i - \frac{\Delta t}{\Delta x}\left(\mathbf{D}^+_{i-\frac{1}{2}} + \mathbf{D}^-_{i+\frac{1}{2}}\right) \; , \tag{26}$$

where the jump terms $\mathbf{D}^{\pm}_{i\pm\frac{1}{2}}$ are computed as

$$\mathbf{D}^{\pm}_{i+\frac{1}{2}} = \mathbf{A}^{\pm}_{i+\frac{1}{2}} \left(\overline{\mathbf{Q}}_{i+1} - \overline{\mathbf{Q}}_{i} \right) \ . \tag{27}$$

Different choices for the matrices $\mathbf{A}^{\pm}_{i+\frac{1}{2}}$ return different path-conservative schemes. Here, for accuracy and generality in the solution, we implement the DOT upwind scheme for non-conservative hyperbolic systems developed by Dumbser and Toro [23], based on a fully-numerical variation of the complete Riemann solver of Osher and Solomon [40].

Following [23,8], we adopt of a simple segment path which connects two states $\overline{\mathbf{Q}}_{i}$ and $\overline{\mathbf{Q}}_{i+1}$ across a discontinuity, i.e.,

$$\boldsymbol{\Psi} = \overline{\mathbf{Q}}_{i} + s \left(\overline{\mathbf{Q}}_{i+1} - \overline{\mathbf{Q}}_{i} \right) \ , \tag{28}$$

with $s \in [0;\ 1]$. The adoption of this path not only is motivated by simplicity, but also, as proven in [23,8], allows the scheme to respect the classical requirement of well-balancedness [2], which prevents the occurrence of non-physical oscillations in the case of still water.

With this path (28), the matrices $\mathbf{A}^{\pm}_{i+\frac{1}{2}}$ of the DOT scheme in (27) read

$$\mathbf{A}^{\pm}_{i+\frac{1}{2}} = \frac{1}{2} \left(\hat{\mathbf{A}}_{i+\frac{1}{2}} \pm \left| \hat{\mathbf{A}}_{i+\frac{1}{2}} \right| \right) \ . \tag{29}$$

System (24) contains non-conservative products and thus classical weak solutions are not defined. However, with the theory developed in [21], a definition of weak solutions is given using a family of paths, e.g. (28). With this insight, $\hat{\mathbf{A}}_{i+\frac{1}{2}}$ in (29) is evaluated as a Roe-type matrix as

$$\hat{\mathbf{A}}_{i+\frac{1}{2}} = \mathbf{A}_{\boldsymbol{\Psi}} \left(\overline{\mathbf{Q}}_{i}, \overline{\mathbf{Q}}_{i+1} \right) = \int_{0}^{1} \mathbf{A} \left(\boldsymbol{\Psi} \left(\overline{\mathbf{Q}}_{i}, \overline{\mathbf{Q}}_{i+1}, s \right) \right) \mathrm{d}s \ . \tag{30}$$

where the integration path is defined (28). In analogous manner, $\left| \hat{\mathbf{A}}_{i+\frac{1}{2}} \right|$ is given by

$$\left| \hat{\mathbf{A}}_{i+\frac{1}{2}} \right| = \left| \mathbf{A}_{\boldsymbol{\Psi}} \left(\overline{\mathbf{Q}}_{i}, \overline{\mathbf{Q}}_{i+1} \right) \right| = \int_{0}^{1} \left| \mathbf{A} \left(\boldsymbol{\Psi} \left(\overline{\mathbf{Q}}_{i}, \overline{\mathbf{Q}}_{i+1}, s \right) \right) \right| \mathrm{d}s \ , \tag{31}$$

with the absolute value of a matrix $|\mathbf{A}|$ defined by

$$|\mathbf{A}| = \mathbf{R} |\boldsymbol{\Lambda}| \mathbf{R}^{-1} \ , \tag{32}$$

where $\mathbf{R}$ is the matrix having as columns the right eigenvectors of $\mathbf{A}$, $\mathbf{R}^{-1}$ is its inverse, and $|\boldsymbol{\Lambda}|$ is the diagonal matrix containing the eigenvalues of $\mathbf{A}$ in absolute value. These linear algebra operations are performed by fully-numerical techniques as suggested in [23]. Finally, the integrals in (30) and

(31) are approximated numerically by means of three-point Gauss-Legendre quadratures, see [23,8].

The use of these fully-numerical integration procedures is crucial for the problem at hand. In fact, analytical computation of the Roe averages (30) and of (31) would be challenging even on the simple path (28), since the size of the system matrix can be in principle arbitrarily increased by including any number N of sediment fractions, and complex non-linear sediment transport relations, e.g. (14), are often employed in the computation of the transport capacity of each fraction.

We observe that, by the use of Gaussian quadrature rules of appropriate order of accuracy, conservation can be practically maintained up to any desired precision [8]. Alternative strategies, not explored in this paper, could be devised to derive schemes which preserve conservation even more accurately. These may involve the use adaptive integration rules, as suggested in [8], or the discretisation of the problem in quasi-conservative form. We present the quasi-conservative formulation of the Saint-Venant-Hirano model and sketch the resulting schemes in Appendix A. However, for the applications of the present paper, we have verified that conservation of sediment mass is maintained up to sufficient precision by our schemes implementing three-point Gaussian quadratures. In detail, by additional tests, we have observed that errors in sediment mass conservation are (by numerous orders of magnitude) smaller than the resolution of data available in the great majority of engineering and geomorphological applications. Therefore, the present schemes appear to be fully applicable in practical cases.

3.2 Administration of size stratification

Up to this point, we have not specified the vertical structure of the substrate and we have only considered a set of integral conservation equations for the total mass of size fractions M_{sk} (7), which have been included in the update formula (26). However, the substrate in general is not vertically mixed. Our implementation includes a bookkeeping procedure for the administration of size stratification and its vertical storage, which is inspired to that documented in [63], and tailored for our numerical solution in the Finite Volume framework (26).

3.2.1 Vertical discretisation of the substrate

The vertical discretisation is sketched in Fig. 2. In each cell $\mathcal{C}_i$ we consider a vertical subdivision of the substrate into n_s sublayers, numbered from bottom to top and indexed with index j, having thickness $L_s(j)$. These sublayers,

unlike the active layer, have fixed vertical displacement. They are built one on top of the preceding one, and the sublayer $j = 1$ has lower interface equal to the assumed (time invariant) elevation datum $\eta_0(x_i)$ in $\mathcal{C}_i$. The number of sublayers n_s can vary at different locations in the domain, i.e., $n_s = n_s(x_i)$.

All the sublayers in the range $1 \leq j < n_s - 1$ have a constant thickness, which is set equal to a default input value L_s^{default}, whereas the top sublayer, located just underneath the active layer, has varying thickness $L_s(n_s)$ in the range $[0, L_s^{\text{default}})$. This thickness value is adjusted to let the elevation of the ceiling of that sublayer match the elevation of the interface between the active layer and the substrate, and thus evolves in time. Having assumed constant active layer thickness (5), the evolution equation for $L_s(n_s)$ is thus analogous to the Exner equation (3), i.e.,

$$\partial_t L_s(n_s) + \partial_x q_b = 0 \; . \tag{33}$$

For each cell $\mathcal{C}_i$ we define a discrete vertical structure of the grainsize distribution in the substrate. Each sublayer is vertically mixed and has an associated grainsize distribution, which is denoted with $f_{sk}(j)$. The vertical profile of grainsize distribution is thus piecewise constant, with discontinuities located at the interfaces between sublayers. The corresponding mass values of the kth fraction are denoted with

$$m_{sk}(j) = L_s(j)\, f_{sk}(j) \; . \tag{34}$$

For each cell $\mathcal{C}_i$, these mass values are related to the total sediment mass in the substrate by

$$M_{sk} = \sum_{j=1}^{n_s} m_{sk}(j) \; . \tag{35}$$

Following the approach of Hirano [26,27], variations in the sediment mass of the substrate, which happen due to rise or drop of the interface with the active layer, affect only the top portion of the substrate, located immediately underneath the interface. Under the assumed vertical discretisation (see Fig. 2), only the grainsize distribution of the top sublayer $f_{sk}(ns)$ shall evolve in time. The resulting equations for sediment mass are

$$\partial_t m_{sk}(n_s) + f_k^I \partial_x q_b = 0 \; , \tag{36}$$

for the top sublayer, and

$$\partial_t m_{sk}(j) = 0 \qquad \text{for } 1 \leq j \leq n_s - 1 \; , \tag{37}$$

for all the others. Notice that equation (36) has identical structure as the conservation equation for the total mass in the substrate (7), and that (36) and (37) after substitution into (35) yield (7).

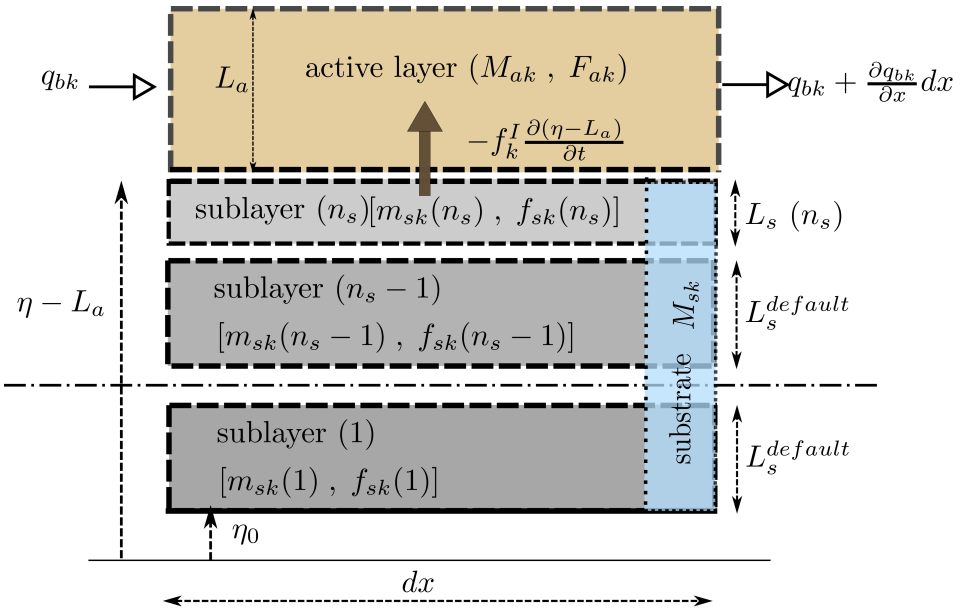

Fig. 2. Sketch and notation of the vertical discretisation of the substrate into n_s sublayers.

The adopted vertical discretisation also allows for specifying the grainsize distribution f_k^I under bed degradation in (8), as the grainsize distribution of the top sublayer $f_{sk}(n_s)$. Equation (8) thus becomes

$$f_k^I = \begin{cases} F_{ak} & \text{if } \partial_t (\eta - L_a) > 0 \\ f_{sk}(n_s) & \text{if } \partial_t (\eta - L_a) < 0 \end{cases} . \tag{38}$$

The changes occurring in the entire substrate affect only the top sublayer, by evolution of its thickness $L_s(n_s)$ governed by (33), and of its grainsize distribution $f_{sk}(n_s)$ governed by (36). Thus, in the numerical solution, we apply the changes in bed elevation η and total mass in the substrate M_{sk} computed by the update formula (26) to $L_s(n_s)$ and $m_{sk}(n_s)$, respectively, and leave the thickness and mass of the other sublayers $1 \leq j \leq N-1$ unaltered. As long as the updated thickness $L_s(n_s)$ stays in the range $[0, L_s^{\text{default}})$, the substrate evolution is entirely determined.

However, if the updated thickness $L_s(n_s)$ falls out of this range, i.e. it is either negative or exceeds the preset value L_s^{default}, then the vertical structure of the bed must be updated in that cell, by reducing or increasing the number of sublayers n_s. These changes are performed in a cell-based manner after the solution to the full IVP (21) has been achieved, and consist in modifying the initial condition for the next integration step. The adopted procedure is mass-conservative.

3.2.2 Degradational cases with consumption of size stratification

Degradational cases with consumption of size stratification are found if $\eta_i^{n+1} < \eta_i^n$ and, after the last time integration, the thickness $L_s(n_s)$ is negative, i.e.,

$$L_s(n_s) < 0 \; . \tag{39}$$

Negative thickness (39) also implies negative mass values $m_{sk}(n_s)$ in the top sublayer. We store these thickness and mass deficits in temporary variables

$$L_s^{\text{deficit}} = -L_s(n_s) \qquad , \qquad m_{sk}^{\text{deficit}} = -m_{sk}(n_s), \text{ for } 1 \leq k \leq N-1 \; . \tag{40}$$

We assume in the present implementation L_s^{deficit} (40) computed in the current time step to have smaller magnitude than the default thickness L_s^{default}, i.e., $L^{\text{deficit}}/L_s^{\text{default}} < 1$. We have verified in our numerical experiments that this assumption is met for physically reasonable values of L_s^{default}, since the explicit time stepping in (25) limits the amount of bed degradation at each time step, and thus the resulting L^{deficit}, to very small values.

To update the vertical structure of the substrate, we proceed as follows. After checking the condition (39) in each $\mathcal{C}_i$, before the next integration step,

- we reduce the number of sublayers n_s by one and thus make the second sublayer from top be the new top sublayer;
- we calculate the thickness of the new top sublayer as

$$L_s\left(n_s\right) = L_s^{\text{default}} - L_s^{\text{deficit}} \; ; \tag{41}$$

- we calculate the mass values of the new top sublayer as

$$m_{sk}\left(n_s\right) := m_{sk} - m_{sk}^{\text{deficit}} \qquad \text{for } \; 1 \leq k \leq N-1 \; . \tag{42}$$

The computed $L_s\left(n_s\right)$ (41) and $m_{sk}\left(n_s\right)$ (42) are positive.

3.2.3 Aggradational cases with creation of size stratification

Aggradational cases with creation of size stratification are found if $\eta_i^{n+1} > \eta_i^n$ and the top sublayer is thicker than the preset thickness value, i.e.,

$$L_s(n_s) > L_s^{\text{default}} \; . \tag{43}$$

We store the values of thickness and sediment mass in the variables

$$L_s^{\text{excess}} = L_s(n_s) \qquad , \qquad m_{sk}^{\text{excess}} = m_{sk}(n_s), \text{ for } 1 \leq k \leq N-1 \; . \tag{44}$$

For simplicity, as in the previous case, we assume L^{excess} to be smaller than L_s^{default}, i.e., $L^{\text{excess}}/L_s^{\text{default}} < 1$, which is fulfilled by the adoption of reasonably thick sublayers, under explicit time stepping (25). We proceed as follows:

- we increase the number of sublayers n_s by 1;
- we compute the thickness of the new top sublayer as $L_s(n_s) = L_s^{\text{excess}} - L_s^{\text{default}}$, and let the formerly top sublayer have thickness $L_s(n_s-1) = L_s^{\text{default}}$;
- we assume the newly-created top sublayer ($j = n_s$) to be initially mixed with the one below ($j = n_s - 1$). Therefore, we split the sediment mass excess (44) among sublayers in amounts proportional to their thickness, i.e.,

$$m_{sk}(j) = \frac{L_s(j)}{L^{\text{excess}}} m_{sk}^{\text{excess}} \qquad \text{for } 1 \leq k \leq N-1, \quad n_s - 1 \leq j \leq n_s \,. \quad (45)$$

3.3 Balancedness of the vertical sediment mass flux under degradation

We introduce here a principle which specifically applies to mixed-sediment morphodynamics governed by the active layer model, and concerns the balancedness of the vertical mass flux between the substrate and active layer under bed degradation. When the bed degrades ($\partial_t \eta < 0$), by the assumed time constancy of the active layer thickness (5), the interface between the active layer and the substrate lowers ($\partial_t (\eta - L_a) < 0$). By equation (8), the active layer approach prescribes that a portion of the substrate having thickness equal to the reduction in the interface elevation, and originally located just underneath the interface, will be consumed, and that an equal volume of sediment having the same grainsize distribution will be transferred to the active layer and mixed with the material available there. The proposed balancedness principle thus states that the grainsize distribution of the vertical mass flux $f_k^I \partial_x q_b$ in equation (7) must exactly match that of the material available at the top of the substrate, even in the discrete schemes (26), not to mistakenly alter the grainsize distribution of the substrate.

To enforce this balancedness principle in our numerical scheme, we shall (i) locate the vertical flux over the cell, (ii) identify the correct grainsize distribution to be used as f_k^I in the numerical scheme, and finally (iii) suitably modify numerical methods to achieve the sought balance.

With respect to (i), we assume the vertical mass flux to be located within each cell $\mathcal{C}_i$, as it is a local vertical process connected to bed degradation within the cell (see Fig. 1). Thus, once the reduction in bed elevation is known by the Exner equation (3), its computation does not involve other horizontal, inter-cell fluxes. Therefore, only data in cell $\mathcal{C}_i$ shall be used to compute the grainsize distribution of this vertical flux f_k^I in $\mathcal{C}_i$, and thus an averaging procedure over a path like (28) shall not apply for f_k^I.

Concerning (ii) in the original model of Hirano [26,27] and earlier numerical implementations, e.g. [46], f_k^I under degradation must be externally imposed,

since the vertical structure of the substrate is not specified, and evolution equations like (7) or (36) are not considered. Here, having adopted a vertical discretisation of the substrate into n_s vertically-mixed sublayers, we set $f_k^I = f_{sk}(n_s)$ in agreement with (38). In the following of this section, we stipulate that the number of sublayers in cell $\mathcal{C}_i$ remains constant and equal to n_s over the current integration step, which implies f_k^I not to vary during that step.

Concerning (iii), in the discrete schemes (26), the balancedness principle is enforced by requiring that, for each $\mathcal{C}_i$, the entries of $\mathbf{D}^{\pm}_{i\mp\frac{1}{2}}$ associated to the evolution of the substrate mass variables (rows $N+3$ to $2N+1$ in the column vectors) are equal to the entry associated to the change in bed elevation (third row), multiplied by the selected fraction values $f_{sk}(n_s)$. This is respected by the DOT scheme after suitable modification. The modified scheme has matrices

$$\mathbf{A}^{\pm}_{i+\frac{1}{2}} = \frac{1}{2}\left(\hat{\mathbf{A}}^{\pm}_{i+\frac{1}{2}} \pm \left|\hat{\mathbf{A}}^{\pm}_{i+\frac{1}{2}}\right|\right) \ . \tag{46}$$

Here two independent evaluations of the Roe-type matrix (30) are required at each cell boundary, namely

$$\begin{array}{l} \hat{\mathbf{A}}^{-}_{i+\frac{1}{2}} = \hat{\mathbf{A}}_{i+\frac{1}{2}}\left(f_{sk}(n_s)_i\right) = \int_0^1 \mathbf{A}\left(f_{sk}(n_s)_i, \mathbf{\Psi}\left(\overline{\mathbf{Q}}_i, \overline{\mathbf{Q}}_{i+1}, s\right)\right) \mathrm{d}s \\ \hat{\mathbf{A}}^{+}_{i+\frac{1}{2}} = \hat{\mathbf{A}}_{i+\frac{1}{2}}\left(f_{sk}(n_s)_{i+1}\right) = \int_0^1 \mathbf{A}\left(f_{sk}(n_s)_{i+1}, \mathbf{\Psi}\left(\overline{\mathbf{Q}}_i, \overline{\mathbf{Q}}_{i+1}, s\right)\right) \mathrm{d}s \end{array} \ , \tag{47}$$

where $f_{sk}(n_s)_i$ and $f_{sk}(n_s)_{i+1}$ are computed within $\mathcal{C}_i$ and $\mathcal{C}_{i+1}$, respectively. The matrices $\left|\hat{\mathbf{A}}^{\pm}_{i+\frac{1}{2}}\right|$ are computed in analogous manner as

$$\begin{array}{l} \left|\hat{\mathbf{A}}^{-}_{i+\frac{1}{2}}\right| = \left|\hat{\mathbf{A}}_{i+\frac{1}{2}}\left(f_{sk}(n_s)_i\right)\right| = \int_0^1 \left|\mathbf{A}\left(f_{sk}(n_s)_i, \mathbf{\Psi}\left(\overline{\mathbf{Q}}_i, \overline{\mathbf{Q}}_{i+1}, s\right)\right)\right| \mathrm{d}s \\ \left|\hat{\mathbf{A}}^{+}_{i+\frac{1}{2}}\right| = \left|\hat{\mathbf{A}}_{i+\frac{1}{2}}\left(f_{sk}(n_s)_{i+1}\right)\right| = \int_0^1 \left|\mathbf{A}\left(f_{sk}(n_s)_{i+1}, \mathbf{\Psi}\left(\overline{\mathbf{Q}}_i, \overline{\mathbf{Q}}_{i+1}, s\right)\right)\right| \mathrm{d}s \end{array} \ . \tag{48}$$

In detail, with the definitions (47), the lines arising from the substrate equations in matrices $\hat{\mathbf{A}}^{\mp}_{i\pm\frac{1}{2}}$, which are used for the solution in cell $\mathcal{C}_i$, are equal to the line of the Exner equation, multiplied by the interface fraction value $f_{sk}(n_s)_i$ in $\mathcal{C}_i$. We have verified that the same relation between the lines of the substrate and that of the Exner equation holds for matrices $\left|\hat{\mathbf{A}}^{\mp}_{i\pm\frac{1}{2}}\right|$ defined by (48). Hence, the requirement for balancedness set above is satisfied by this modified method.

Noteworthy, degradational (and aggradational) conditions should be identified in advance, in order to apply the correct interface fraction values $f_{sk}(n_s)_i$ in case of degradation. This would require anticipated knowledge of the sign of the variation in bed elevation in each cell during the current time step, prior

to the solution of the active layer and substrate mass conservation equations, which is impossible since in the present schemes all the variables are updated simultaneously. Therefore, here we adopt an iterative implementation of numerical schemes, as follows:

(1) the solution to IVP1 (22) is computed for all cells;
(2) aggradational conditions are assumed throughout the domain and IVP2 (23) is solved in all cells;
(3) if bed degradation occurs in cell $\mathcal{C}_i$, IVP2 (23) is solved again in that cell assuming degradational conditions.
(4) IVP3 is solved and the solution advances by a full time step Δt.

The possibility of correcting the solution in cell $\mathcal{C}_i$ independently from the neighbouring cells is guaranteed by the adoption of two independent Roe-type matrices (47) over each cell edge.

The balancedness principle defined above is violated only when bed degradation is such that one sublayer in the substrate is removed (see Section 3.2), since the grainsize distribution $f_{sk}(n_s)_i$ used for computing the vertical mass flux could differ from that of the sediment mass in the second-upper sublayer $f_{sk}(n_s-1)_i$. As a consequence, only upon reduction of the number of sublayers, the grainsize distribution in the new top sublayer may be modified. Still, anyway, the grainsize distribution of the vertical flux is computed within the current cell, as required. To balance the numerical scheme even this case, i.e. to exactly capture the piecewise-constant behaviour of the grainsize distribution in the substrate, very high-order accuracy in time integration would be needed. However, for practical applications, we have verified that the drawback is not severe, since the error is limited to one sublayer (i.e., it does not affect the full substrate) and is encountered only occasionally, provided the default thickness of sublayers L_s^{default} is set reasonably higher than the amount of bed degradation in a time step, as required in Section 3.2.

Under aggradational conditions ($\partial_t \eta > 0$), the requirement for balancedness of the mass flux between the active layer and the substrate is physically less stringent. In fact, alternative relations to (8), (38) yield f_k^I as a weighted average between the grainsize distribution of the sediment in the active layer and that of bedload, see [43,28,60]. Nonetheless, for consistency, we still employ the same modifications described above even under aggradation. Thus, the grainsize distribution in the vertical mass flux is still evaluated in a cell-based manner within $\mathcal{C}_i$ using the appropriate fraction values $f_k^I = F_{ak}$ computed with the data $\overline{\mathbf{Q}}_i$.

Finally, it is worth mentioning that the balancedness of the vertical mass flux under degradation is relevant also for other models for mixed-sediment morphodynamics which include an administration procedure for size stratification.

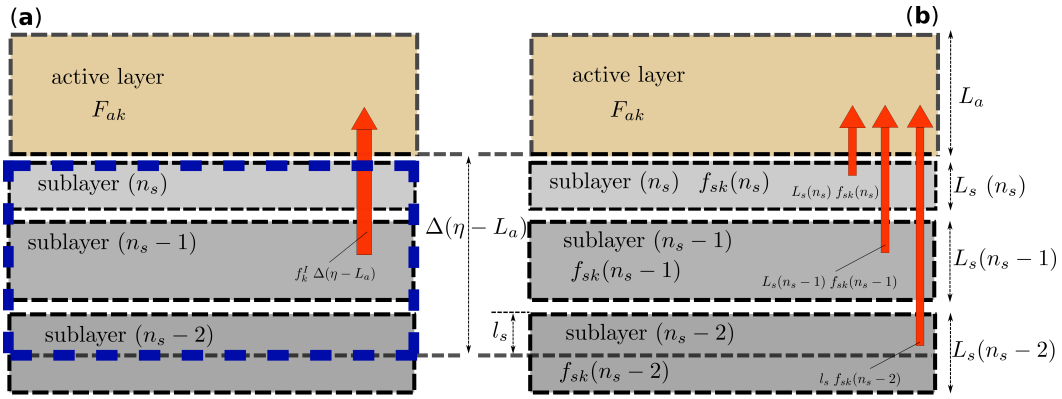

Fig. 3. Application of the balancedness concept for the vertical sediment mass flux under bed degradation, for a generic model. The model here illustrated has piecewise-continuous description of the vertical sorting profile and, unlike our model, is able to consume an arbitrary number of sublayers in a time step. (a): integral formulation of the vertical mass flux; (b): components of the vertical mass flux, for each sublayer consumed under degradation.

For clarity, in Fig. 3 we show an application of the balancedness principle to a generic numerical model with piecewise-continuous description of the vertical sorting profile. The considered model is balanced under degradation and, unlike our model, is able to consume an arbitrary number of sublayers in the substrate in a single time step. In detail, as indicated by the blue dashed contour in Fig. 3a, while the interface elevation reduces by $\Delta\left(\eta - L_a\right)$, the degradation process entirely consumes two sublayers ($j = n_s$ and $j = n_s - 1$) and partially affects sublayer $j = n_s - 2$. Moving to Fig. 3b, to satisfy the mass conservation principle for each size fraction, the grainsize distribution of the vertical flux f_k^I shall be computed as a weighted average of the grainsize distribution of each sublayer totally or partially consumed during that time step, with weights based on the thickness of the (portions of) sublayers consumed, i.e.,

$$f_k^I = \frac{L_s\left(n_s\right) f_{sk}\left(n_s\right) + L_s\left(n_s - 1\right) f_{sk}\left(n_s - 1\right) + l_s f_{sk}\left(n_s - 2\right)}{\Delta\left(\eta - L_a\right)}\,, \tag{49}$$

with $l_s = \Delta\left(\eta - L_a\right) - L_s\left(n_s\right) - L_s\left(n_s - 1\right)$.

Noticeably, in existing codes, though not explicitly formulated, the proposed balancedness concept is often straightforwardly assumed. For instance, by stating that "if the flow erodes material from the bed, the substrate grain size distribution does not change", Viparelli *et al.* [63] implicitly assume their scheme to be balanced, and thus conveniently remove the need of updating the grainsize distribution of the substrate under degradation.

3.4 Second order extension

We extend the basic first-order DOT scheme to second-order accuracy in space and time in the ADER-ENO framework, e.g. [59,25]. The key components in our second order extension are

- a piecewise linear reconstruction of data, whereby slopes are obtained by the Essentially Non Oscillatory (ENO) approach, e.g. [25];
- a cell-based space-time evolution procedure in the ADER framework, e.g., [59];
- a fully-discrete explicit second-order accurate update formula.

Next, we will briefly revise these components and point out some peculiarities in the present implementation.

A piecewise-linear reconstruction polynomial in all variables reads

$$\mathbf{w}_i = \overline{\mathbf{Q}}_i + \mathbf{a}_i \left(x - x_i\right) \ , \tag{50}$$

where the reconstruction slope $\mathbf{a}_i$ is achieved following the ENO approach as

$$\mathbf{a}_i = \frac{1}{\Delta x} \text{minmod} \left(\overline{\mathbf{Q}}_i - \overline{\mathbf{Q}}_{i-1}, \overline{\mathbf{Q}}_{i+1} - \overline{\mathbf{Q}}_i \right) \ , \tag{51}$$

and the minmod function of two real arguments returns the argument characterised by the lowest absolute value. Equations (50) and (51) are applied component-wise to the first $N+2$ conserved variables in vector $\mathbf{Q}$ (18), i.e. to water elevation H, flow discharge q, bed elevation η and the sediment mass variables in the active layer M_{ak} (for $1 \leq k \leq N-1$).

Adoption of a non-linear reconstruction (50) for the mass variables in the active layer M_{ak} also implies that the active layer thickness L_a can no longer be spatially constant. In fact, if, for consistency, for the mass Nth fraction M_{aN} (11) an analogous reconstruction to that in (50) is adopted, then also L_a must have a piecewise-linear structure to respect the constraint (10) . In second-order schemes we thus use

$$\left(L_a\right)_i = L_a + a_L \left(x - x_i\right) \tag{52}$$

where a_L is given by the sum of the reconstruction slopes for all the mass variables M_{ak} (for $1 \leq k \leq N$). Equation (52) does not imply that temporal constancy of the active layer thickness is violated, and equation (5) still holds throughout the cell $\mathcal{C}_i$ in the current time step for the reconstructed active layer thickness (52).

For the last $N-1$ entries of $\mathbf{Q}$ (18), representing the mass variables in the substrate M_{sk} (for $1 \leq k \leq N-1$), a piecewise-linear reconstruction is not

needed. In fact, the reconstructed gradients of M_{sk} would not affect the time evolution of any variable in $\mathbf{Q}$, as the corresponding entries in $\mathbf{A}$ (20) (last $N-1$ columns) are null. For these variables we thus adopt

$$\mathbf{a}_i = \mathbf{0}\,, \tag{53}$$

without any loss of accuracy in the second-order extension. This choice enables preserving the balancedness concept with the procedure detailed in Section 3.3 without further complications, even for second-order accurate schemes.

The key idea in the ADER approach is to solve high-order Riemann problems at the element boundaries. This is achieved using a space-time Taylor series expansion. For second-order schemes, a first-order expansion is sufficient, i.e.,

$$\mathbf{Q}_i\left(x,t\right) \approx \overline{\mathbf{Q}}_i + \left(x-x_i\right)\partial_x \mathbf{Q}|_{\overline{\mathbf{Q}}_i} + \left(t-t^n\right)\partial_t \mathbf{Q}|_{\overline{\mathbf{Q}}_i}\,. \tag{54}$$

To evaluate the time derivatives in (54) as functions of space derivatives, the Cauchy-Kowalevski procedure is used. For second-order accuracy it suffices to rewrite the system (24) as

$$\partial_t \mathbf{Q} = -\mathbf{A}\partial_x \mathbf{Q}\,. \tag{55}$$

The value of $\mathbf{Q}_i\left(x,t\right)$ and its spatial derivatives are obtained from the reconstruction polynomial (50). In our implementation, the Taylor expansion (54) is performed twice, assuming aggradational and degradational conditions in matrix $\mathbf{A}$ in (55), i.e., using the values $f_k^I = F_{ak}$ and $f_k^I = f_k(n_s)$, respectively (38), and two corresponding values of the space-time polynomial $\mathbf{Q}_i(x,t)$ (54) are computed.

Once the Taylor expansion (54) has been performed for each cell, the final second-order accurate one-step scheme reads

$$\begin{aligned}
&\overline{\overline{\mathbf{Q}}}_i = \overline{\mathbf{Q}}_i \\
&-\tfrac{1}{\Delta x}\int_{t^n}^{t^{n+1}}\int_{x-\frac{1}{2}}^{x+\frac{1}{2}} \mathbf{A}\left(\mathbf{Q}_i\left(x,t\right)\right)\partial_x \mathbf{Q}_i\left(x,t\right)\mathrm{d}x\mathrm{d}t \\
&-\tfrac{\Delta t}{\Delta x}\left(\mathbf{D}^+_{i-\frac{1}{2}} + \mathbf{D}^-_{i+\frac{1}{2}}\right)\,,
\end{aligned} \tag{56}$$

with

$$\begin{aligned}
\mathbf{D}^+_{i-\frac{1}{2}} &= \tfrac{1}{\Delta t}\int_{t^n}^{t^{n+1}} \mathbf{A}^+_{i-\frac{1}{2}}\left(\mathbf{Q}_i\left(x_{i-\frac{1}{2}},t\right) - \mathbf{Q}_{i-1}\left(x_{i-\frac{1}{2}},t\right)\right)\mathrm{d}t \\
\mathbf{D}^-_{i+\frac{1}{2}} &= \tfrac{1}{\Delta t}\int_{t^n}^{t^{n+1}} \mathbf{A}^-_{i+\frac{1}{2}}\left(\mathbf{Q}_{i+1}\left(x_{i+\frac{1}{2}},t\right) - \mathbf{Q}_i\left(x_{i+\frac{1}{2}},t\right)\right)\mathrm{d}t
\end{aligned}\,. \tag{57}$$

where the balanced matrices (46) are used. In our implementation, space and time integrals in (56) and (57) are computed using a very compact midpoints rule (i.e., one-point Gauss-Legendre quadratures), as in [55].

As for first-order cases, proper identification of aggradational and degradational cases requires an iterative implementation of the update formula, as

detailed in Section 3.3. A last remark concerns the values f_k^I (38) to be used in the evaluation of matrices in (56) and (57). Under aggradational conditions, we use the grainsize distribution in the active layer F_{ak}, computed with the output of the ADER evolution procedure (54), evaluated at the required time and space nodes over the Gaussian quadratures. Under degradational condition, we simply use the grainsize distribution in the top sublayer of the substrate $f_{sk}\left(n_s\right)_i$ evaluated with the initial data at time t^n. This is allowed because in this case the grainsize distribution of the substrate is supposed not to vary in time during the evolution step (see Section 3.3), and, having assumed null reconstruction slopes in the substrate (53), it is also spatially constant within cell $\mathcal{C}_i$. With these considerations, provided n_s stays constant during the current time step, the second-order scheme (56) is balanced under bed degradation.

4 Applications

In this section we will apply the proposed numerical solutions to three test cases. First, we will observe the model performance under bed degradation and highlight the importance of the balancedness of vertical sediment mass fluxes, by comparison with a non-balanced scheme. In the second test case we will assess the model capability of addressing the propagation of small-amplitude hydro-morphodynamic waves, by comparison with the analytical linearised solution developed in [54]. The last test case is about the numerical reproduction of flume experiment E8-E9 by Ribberink [46], which concerns the morphodynamic adjustment of a bed covered by dunes, and includes bed elevation changes and streamwise and vertical sorting.

4.1 Bed degradation and armouring: balancedness of vertical mass fluxes

To show the importance of the balancedness requirement in Section 3.3, and that our code is able to respect it, we perform here a test on the development of bed armouring under degradation due to lack of sediment supply.

We assume a $100\,m$ long channel with specific discharge $q = 0.5\,m^2 s^{-1}$ and slope 0.08%. The sediment mixture is strongly bimodal and discretised with two fractions, with diameters $d_1 = 0.001m$ and $d_2 = 0.01m$. The bed is initially composed of the fine fraction by 70% throughout the domain. The resulting grainsize distribution at initial time is constant over the vertical direction. This is illustrated in Fig. 4a, where we show the initial volume fraction content of the fine fraction in the active layer (F_{a1}) and in the substrate (f_{s1}), in the first cell of the domain, at $x = 0.5\,m$, as function of the vertical coordinate z. For

reference, in the same figure, the displacement of the active layer and of the substrate is also indicated.

We model sediment transport by the relation (14) with $A = 8$, $B = 3/2$, $\theta_c = 0.047$, $\epsilon = 0.4$, including the hiding-exposure correction (16), and setting the dimensionless Chèzy coefficient $C = 10$ in (15). Under the assumption of plane bed conditions, we prescribe $\mu = 1$ in (15) and active layer thickness $L_a = 3\,cm$, which corresponds to 3 times the coarsest diameter in the mixture. We discretise the substrate into sublayers having maximum thickness $L_s^{\text{default}} = 1\,cm$.

Flow is subcritical. The downstream boundary condition imposes constant free-surface elevation, which initially corresponds to a water depth $h = 0.574m$. This sets a slightly accelerated backwater profile of the M2 type, see, e.g., [15, see, e.g.,]. Over the upstream boundary, we impose null sediment income, $q_b = 0$, and a constant flow discharge $q = 0.5\,m^2s^{-1}$. We solve the problem at $t = 1800\,s$ in the domain $[0, 100]$ m discretised with 100 cells, using $CFL = 0.9$ in (25). We employ the balanced DOT scheme in first and second-order accurate setup, and we compare its performance to a non-balanced first-order solution by the DOT scheme. The latter is obtained by using a path-averaged value for the grainsize distribution f_k^I (38) for the computation of the jump terms (46).

Results are displayed in Fig. 4c-d. In each figure, we present the vertical sorting profiles computed at final time over the first cell of the domain, at $x = 0.5\,m$, where degradation is most evident, and we indicate the vertical displacement of the active layer and substrate. In detail, the solution of the first-order balanced scheme (Fig. 4b), of the second-order balanced scheme (Fig. 4c), and of the first-order non-balanced scheme (Fig. 4d) are presented.

The solution of all schemes exhibits marked bed degradation caused by lack of sediment supply at the upstream end, and coarsening of the active layer due to selective transport. Coarsening is indicated by the decreased content of the fine fraction F_{a1}, to values smaller than 0.5, with respect to the initial value $F_{a1} = 0.7$. Focussing on the balanced schemes, the first-order scheme in Fig. 4b and the second-order scheme in Fig. 4c provide analogous results, although the second-order solution is characterised by more intense coarsening, due to the sharper longitudinal sorting profiles which result from the lower numerical dissipation of a second-order scheme. Over the degradation process, both balanced schemes are able to keep the grainsize distribution of the substrate visually unaltered and equal to the initial value $f_{s1} = 0.7$.

This is not the case for the non-balanced scheme in Fig. 4d, the solution of which shows a marked spurious overshoot up to about $f_{s1}(n_s) = 0.85$. Although this problem is only found in the top sublayer at that time, it is

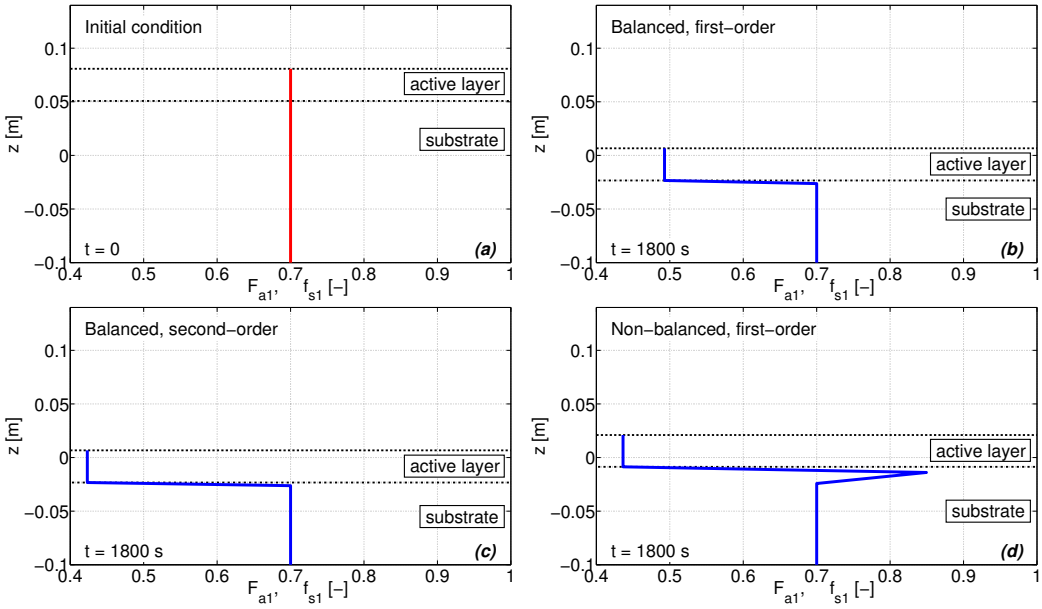

Fig. 4. Bed degradation and armouring: balancedness of vertical mass fluxes. The vertical profiles of the volumetric fraction content of the fine fraction in the substrate (f_{s1}) and active layer (F_{a1}) are presented. The initial condition and the results of three numerical schemes at $t = 1800\,s$ are compared. (a) initial condition; (b) first-order balanced DOT scheme; (c) second-order balanced ADER-ENO DOT scheme; (d) first-order non-balanced DOT scheme.

severe, and potentially misleading in the physical interpretation of results. We have also verified that the non-balanced scheme repeatedly computes negative fraction values in the substrate, due to its inability in matching the vertical mass flux exiting the top sublayer with the extent of bed degradation in the same cell. Even though we have let the computation run with these negative values, we observe that this represents a conceptual drawback, and potential threat for stability of the model. Conversely, the positivity of fraction values was always respected by the balanced schemes. These observations show the importance of using balanced schemes for bed degradation, and motivate our modification of the DOT scheme (46).

4.2 Dynamics of infinitesimal-amplitude hydro-morphodynamic waves for multiple sediment fractions

With this test we aim at assessing the accuracy of the DOT scheme in the solution to the system of governing equations, employing a purely mathematical benchmark. The setup is highly idealised. It concerns the propagation of small-amplitude hydro-morphodynamic waves in the case of a multiple-fraction mixture, triggered by a localised initial imbalance in the grainsize distribution of the active layer, in absence of friction.

A linearised analytical solution, presented in [54], is available, and will be used to assess the convergence of our numerical solution. Noteworthy, unlike most applications of the Hirano model, which are tested with laboratory or field data and thus depend on the calibration of friction and sediment transport, which introduces some degree of empiricism in the computations, the present benchmark is free from calibration issues. This makes the test more severe from a numerical perspective. We thus propose this case with analytical solution as a standard benchmark for numerical solutions to the Saint-Venant-Hirano model.

As further benchmark, we implement another synchronous numerical solution by the PRICE-C centred method of Canestrelli *et al.* [8], which is more diffusive than DOT.

4.2.1 Setup

The setup used in this section is analogous to that presented in [54][section 4.2.3], apart from differences in the values of reference dimensionless parameters and in the transport model. We consider a 40 meter long, flat-bottom horizontal channel, characterised by a plane, erodible bed composed of mixed sediment. The sediment mixture is discretised using $N = 5$ size fractions, with sediment diameters $d_1 = 0.1\,mm$, $d_2 = 8\,mm$, $d_3 = 15\,mm$, $d_4 = 22\,mm$, $d_5 = 29\,mm$.

Flow, from negative to positive x, is subcritical, with constant discharge. In this idealised case, friction in the momentum equation (2) is neglected, i.e., flow is inviscid. For setting uniform flow and sediment transport throughout the domain, we define an unperturbed reference state of variables, which are indicated in the following with subscript R. The reference depth and velocity are $h_R = 1\,m$ and $u_R = 2.035\,ms^{-1}$, which give reference Froude number $Fr_R = 0.65$. The reference grainsize distribution in the active layer is $F_{ak} = F_{aR}$ for all fractions, with $F_{aR} = 1/N = 0.2$. For computing sediment transport, we use the bedload relation (14), with $A = 8$, $B = 3/2$, $\theta_c = 0.047$, and $\epsilon = 0.4$. Unlike Stecca *et al.* [54], we do not apply a hiding-exposure correction (16), i.e., we set $\xi_k = 1$. Neglect of the hiding effect in the present exercise aims at achieving a higher spread in the transport capacities of each fraction. This in turn enhances the difference in speed between the distinct waves carrying a streamwise sorting signal (see Section 4.2.2), to better appreciate their separation. In the computation of the Shields stress of each fraction (15) we use ripple factor $\mu = 1$ and Chèzy coefficient $C = 10.4$. For these values, the ψ parameter, defined as

$$\psi = \frac{\partial q_b}{\partial q}\,, \tag{58}$$

which measures the intensity of bedload in the flow in the linearised analyses of morphodynamic models, e.g. [54,35,32,34,46,22], for the reference state assumes the value $\psi_R = 0.0075$, indicating high sediment transport [54,34,32]. Therefore, all fractions are mobile.

We set computational domain in the range $x \in [-20; 20]$ and timeout $t = 100s$. The initial condition, given by

$$\begin{cases} h\left(x,0\right) = h_R \quad , \quad u\left(x,0\right) = u_R \quad , \quad \eta\left(x,0\right) = 0 \ , \\ \begin{cases} F_{a2}\left(x,0\right) = F_{aR} + A_F \exp\left(-\left(\frac{x}{\sqrt{2}\sigma}\right)^2\right) \ , \\ F_{ak}\left(x,0\right) = F_{aR} - \frac{1}{4}A_F \exp\left(-\left(\frac{x}{\sqrt{2}\sigma}\right)^2\right) \quad \text{for } k = 1,3,4 \end{cases} \\ f_{sk}\left(x,z,0\right) = F_{ak}\left(x,0\right) \quad \text{for } 1 \leq k \leq 5 \ , \end{cases} \ , \tag{59}$$

is assumed equal to the reference state throughout the domain, except for a localised perturbation in the grainsize distribution in the active layer F_{ak}, located around $x = 0$ (i.e., at the domain centre), having Gaussian shape, with standard deviation $\sigma = 0.2035\, m$. The amplitude of the perturbation is very small, so as to comply with the hypothesis of linearity, under which the analytical solution is derived [54]. In detail, a localised increase of the content of the second fraction F_{a2} of amplitude $A_F = 0.001$ is applied, whereas the perturbation in all the other fractions has amplitude $-A_F/4$. Finally, the initial grainsize distribution in the substrate f_{sk} is assigned equal to that in the active layer at the same location. In the present flat-bed case, the active layer thickness is chosen equal to 4 times the average diameter, $L_a = 0.06\, m$. Since the analytical solution in [54] focuses on streamwise, and not on vertical, sorting, indication on the substrate thickness and layering is not provided there. Here we adopt a single, vertically-mixed sublayer in the substrate ($n_s = 1$), having initial thickness equal to that of the active layer. The choice does not affect the numerical solution in any significant manner, as in the present test changes in bed elevation, and thus vertical mass exchanges, are very small.

4.2.2 Linearised wave dynamics

At $t = 0$, the imbalance in sediment transport associated to the perturbation described by (59) triggers hydro-morphodynamic waves, which propagate through the domain at different speed. We give here a brief description of such wave propagation based on the analysis in [54], to which we refer the reader for further detail. The model set for $N = 5$ fractions describes in total $2N + 1 = 11$ waves, each one corresponding to one of the eigenvalues of the system matrix (20). $N - 1$ of these waves, which correspond to the null eigenvalues introduced by the substrate equations (7), are steady, and locally retain the information on the grainsize distribution of the substrate. Under

the assumed high transport conditions, whereby all the sediment fractions are transported, all the remaining $N+2$ waves carry perturbations in all the hydrodynamic and morphodynamic variables. Within this subset, we particularly focus on the waves which carry most morphodynamic changes, namely the "bed" wave and the $N-1=4$ "sorting" waves as defined in [54]. The "bed" wave under well-developed subcritical conditions is described by any morphodynamic model based on the Exner equation (3), even when a single sediment size is considered [22,35], while the "sorting waves" are specifically related to the introduction of active layer equations (6) for mixed sediment [54,49,46].

Under the present subcritical flow conditions, the "bed" and "sorting" waves are all downstream-travelling and, for the commonly assumed setup of the active layer thickness, the "sorting" waves are faster than the "bed" wave [46,49,52,54]. The "sorting" waves carry most of the initially-imposed perturbation in the grainsize distribution of the active layer, while travelling at distinct, albeit close pace, and separating. This in our setup results in 4 distinct streamwise sorting signals. Each of these travelling perturbations of the grainsize distribution of the active layer generates a local perturbation of the flat bed profile, due to the associated imbalances in total bedload transport. This in turn triggers two feedback effects. First, in order to retain the balance in total sediment mass, which is guaranteed by the Exner equation (3), an additional perturbation in bed elevation is generated and carried along the "bed" wave. Secondly, each of these perturbations causes a perturbation of the hydrodynamic variables, which locally affects the flow depth profile.

4.2.3 Results

We solve (17)-(20) using a coarse mesh of 500 cells and a fine mesh of 4000 cells, with transmissive boundary conditions and $CFL=0.9$ in (25). We employ the proposed DOT scheme, both in first-order setup (26) and in second-order ADER-ENO extension (56), which we compare with the linearised analytical solution [54]. The competing PRICE-C scheme [8], is also implemented in identical second-order extension. Noteworthy, the features of these two schemes have been recently compared in [48] for another system of PDEs.

The numerical profiles of the DOT and PRICE-C schemes are compared to the analytical solution in Figs. 5 and 6, respectively. The displayed profiles report the deviation of the solution from the reference values of variables. First-order solutions are reported by thin full grey lines, second-order solutions by dashed coloured lines. Both for first-order and second-order schemes, the solution obtained using a coarse mesh ($N=500$ cells) and a fine mesh ($N=4000$ cells) are compared. The analytical solution [54] is reported by a thick grey line. The view in the solution profiles is limited to the region of the domain where the

waves which carry significant morphodynamic changes are located. These are the "bed" wave at $x \sim 2.3\,m$ and the four "sorting" waves at $x \sim 3.5\,m$, $x \sim 5.2$, $x \sim 7.1$, $x \sim 9.3$. All these waves are revealed in the analytical solution by smooth perturbations in the flow depth and bed profiles, while only the "sorting" waves carry appreciable changes in the grainsize distribution of the active layer.

The reproduction of this pattern of perturbations is a severe test for numerical solvers. The solver shall be able to capture the speed of each wave, and, for each of them, it must correctly detect the complex interactions and feedbacks among the various parts of the system. To clearly discern all the distinct travelling perturbations, numerical dissipation must be limited as much as possible. This is particularly challenging since the waves which carry most of the hydro-morphodynamic interactions, with which we are concerned here, are typically not the fastest waves in the set [54]. In this respect, upwind schemes based on complete Riemann solvers, like the DOT scheme, generally perform better than genuinely centred schemes like PRICE-C. In fact, complete upwind methods resolve intermediate waves independently, assigning a different amount of dissipation to each of them, whereas centred schemes compute numerical dissipation so as to satisfy a stability condition (25) based on the fastest wave in the set, and then straightforwardly apply it also to the slower waves, thus causing excessive diffusion in the associated fields.

In Fig. 5, the solutions of DOT are proven to converge to the reference solution when the mesh is refined and a second-order scheme is employed. In detail, first-order solutions are affected by excessive numerical dissipation, and thus visibly characterised by smearing of perturbations and spurious damping in correspondence to their peaks. While the first-order solution obtained on a fine mesh is unable to display all the distinct perturbations, the resolution significantly improves with a mesh refinement. Moving to second-order solutions in Fig. 5, the accuracy achieved on a coarse mesh is generally analogous to that of the first-order solution on the fine mesh. This means that the gain in accuracy given by the use of a second-order scheme is comparable to that associated to a mesh refinement by a factor 8 in this test, which clearly motivates the effort in the implementation of the ADER extension. Finally, combining second-order accuracy and a fine mesh, the numerical solution almost matches the analytical solution.

The solutions of the PRICE-C scheme in Fig. 6 are generally plagued by excessive spurious dissipation, as expected. First-order solutions at any grid resolution are not able to reproduce even the basic features of the analytical solution profile, and smooth out all the travelling perturbations associated to hydro-morphodynamic waves. The resolution improves by the use of a second-order extension of PRICE-C. However, the second-order solution on a coarse mesh is still unable to clearly identify the four perturbations associated to

Table 1
Convergence to the linearised wave propagation solution for $N = 5$ fractions under subcritical flow conditions: comparison of wallclock times (in seconds) for the DOT and PRICE-C scheme in second and first order setup.

	PRICE-C		DOT	
n_c	first order $t_{CPUs}\,(s)$	second order $t_{CPUs}\,(s)$	first order $t_{CPUs}\,(s)$	second order $t_{CPUs}\,(s)$
250	7.9E1	9.1E1	4.4E2	6.2E2
4000	3.9E3	5.2E3	2.7E4	3.1E4

each "sorting" wave, and only using a fine mesh all the distinct perturbations in all variables can be discerned. Comparing the two schemes, the first-order solutions of DOT in Fig. 5 are closer to the analytical solution than the second-order solutions of PRICE-C in Fig. 6 on the same mesh. This definitely motivates the choice of a refined upwind approach, rather than of a simpler, but less accurate, centred approach.

Finally, in Tab. 1 we show the computational times needed to accomplish these simulations. We ran all computations in double precision on one single CPU core of an Intel Core I5 processor with 2.5 GHz clockspeed. As a drawback of its superior accuracy, the DOT method appears to be about six times more expensive than the PRICE-C method. In this respect, the present test is quite challenging for the DOT scheme, in that the adopted 5 fraction-setup produces a system matrix of size 11×11, the eigenstructure of which is very cumbersome to be computed numerically. This is not generally the case in many morphodynamic computations, for which a two or three-fraction setup is used, and thus the overhead of using an upwind method will be lower. Anyway, the computational performance of DOT could be significantly improved by implementing the technique recently developed by Castro *et al.* [12], by which the viscosity matrix is approximated without explicitly computing the system matrix eigenstructure. Finally, the results in Tab. 1 also show that using a second-order extension is a relatively cheap improvement, as the computational time increases by less than a factor 2 with respect to that of first-order schemes.

4.3 Vertical and streamwise sorting in a bedform-dominated experimental case

In this test we numerically reproduce the flume experiment E8-E9 by Ribberink [46], which is about the transition between an initial and a final equilibrium state, induced by progressively coarsening the sediment feed. To our knowledge, model reproductions of this setup have been performed only in [46,3]. In detail, in [3], the performance of Hirano's active layer model was compared with that of three more refined mixed-sediment continuity models for sorting due to bedforms. These modelling attempts will serve as bench-

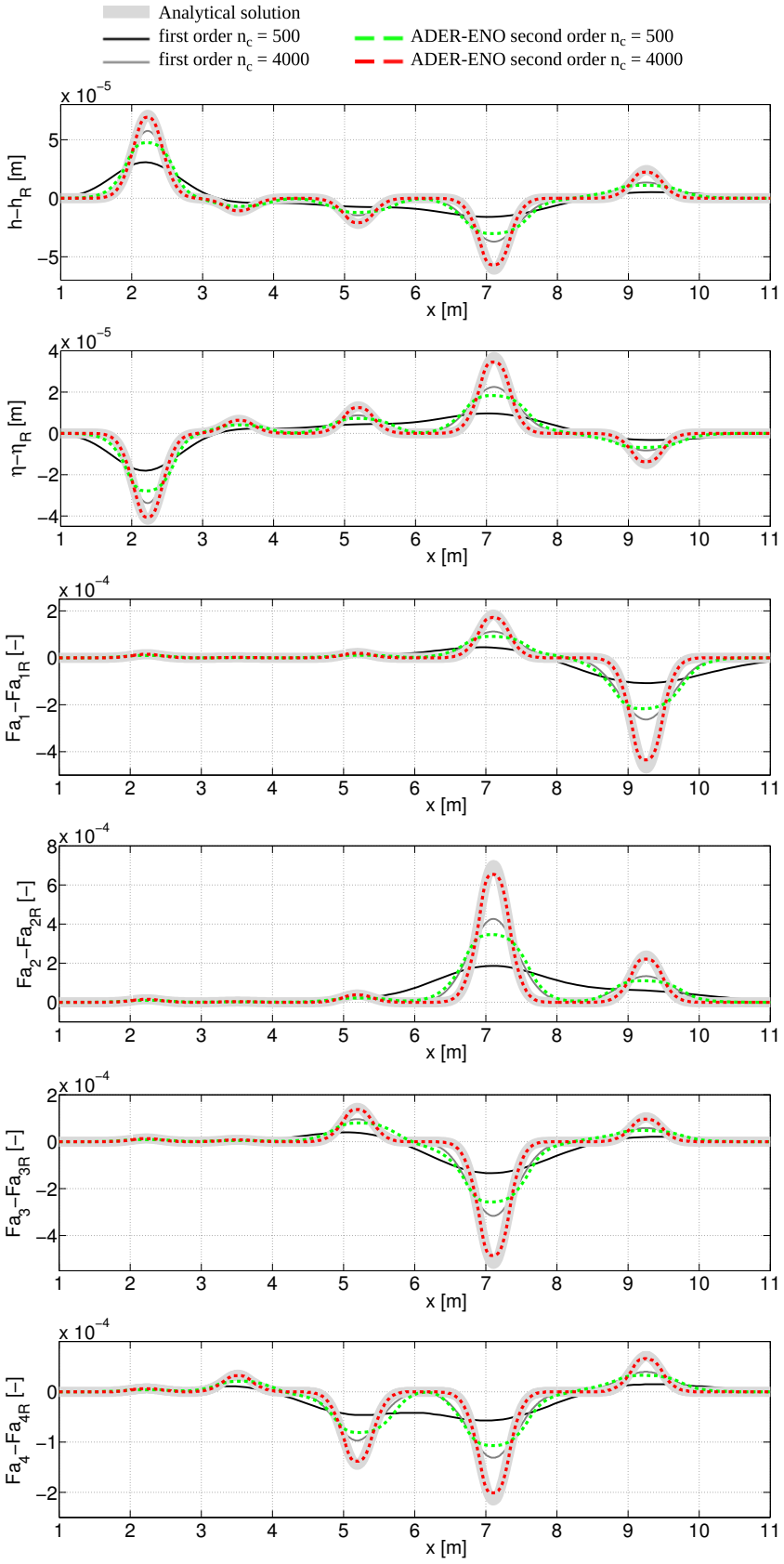

Fig. 5. Convergence to the linearised wave propagation solution for $N = 5$ fractions under subcritical flow conditions for the DOT scheme. Results are presented at $t = 100\ s$.

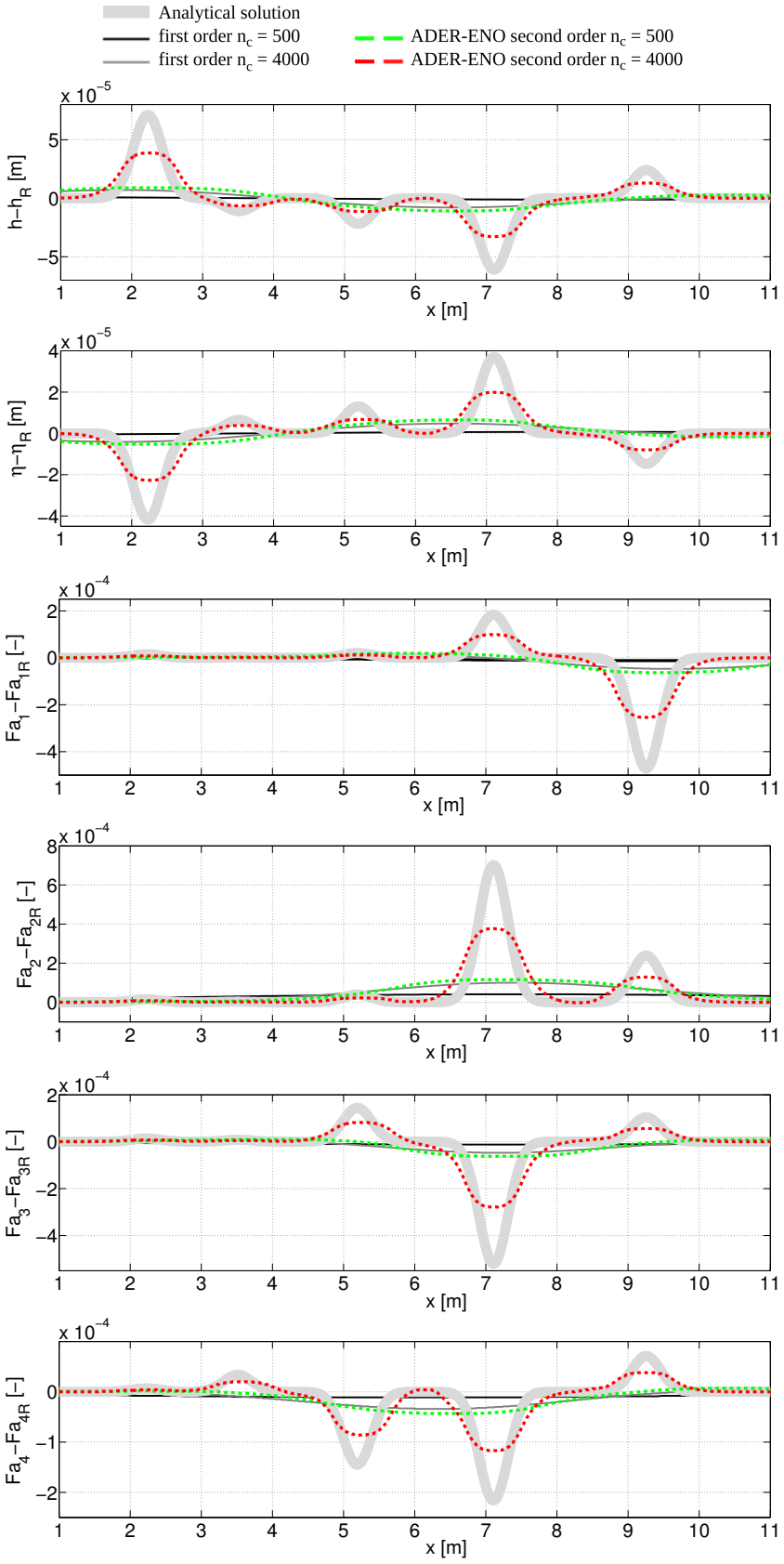

Fig. 6. Convergence to the linearised wave propagation solution for $N = 5$ fractions under subcritical flow conditions for the PRICE-C scheme. Results are presented at $t = 100\ s$.

mark for our accurate solution based on the DOT scheme. Besides these, we will also compare the performance of the DOT and PRICE-C scheme.

This exercise is relevant in three respects. (i) First, on the side of the numerical solution, it represent a test on the model accuracy, in that spurious dissipation must be limited to capture the amplitude and propagation speed of morphodynamic changes, over a relatively long computational time. (ii) Second, from the physical point of view, the numerical solution can be combined with the outcomes of linearised analyses [46,54] to provide insight on the propagation of morphological changes for a real-world case. (iii) Last, concerning the underlying mathematical model, once inaccuracies of numerical origin have been limited, the match between the model outcomes and laboratory data will highlight the strength and limitations of the active layer approach to mixed-sediment continuity modelling.

In these three respect, we will show (i) that the solution of DOT improves accuracy with respect to the previous solution of the active layer model in [3] and to the solution of PRICE-C in the description of streamwise sorting processes and associated bed elevation changes, and that this improvement is relevant to achieve a better match with the experimental data; (ii) that the celerity of streamwise morphodynamic processes can be explained by the outcome of linear analyses over relatively short times, but their changing amplitude requires a non-linear explanation; (iii) that the active layer model is adequate for the description of streamwise sorting processes in the present test case, but over-simplified with respect to vertical sorting and size stratification, and that these physical shortcomings cannot be cured by improved numerics.

4.3.1 Flume experiment and numerical setup

The experiment was performed in a 30 meter long flume. The sediment mixture consisted of two sand fractions (grain sizes $d_1 = 0.78\,mm$ and $d_2 = 1.29\,mm$), which gave rise to grainsize-selective transport. The bed was covered by dunes, the height of which slightly decreased from $3.3\,cm$ to $2.9\,cm$ during the experiment. The flow discharge was constant ($q = 0.0803 m^2 s^{-1}$) and the downstream water depth was steady and equal to $0.167\,m$. The run started from an equilibrium condition, whereby the initial bed slope was constant and equal to 0.165%. Initially, the vertical sorting profile was characterised by a downward coarsening trend. This is represented by square markers in Fig. 7, where the content of the fine fraction measured at the downstream end of the flume is reported as function of the vertical coordinate z, replotted from the original data [46]. The vertical sorting profile was measured with vertical resolution of $5\,mm$.

The time development of sediment supplied to to the flume is represented

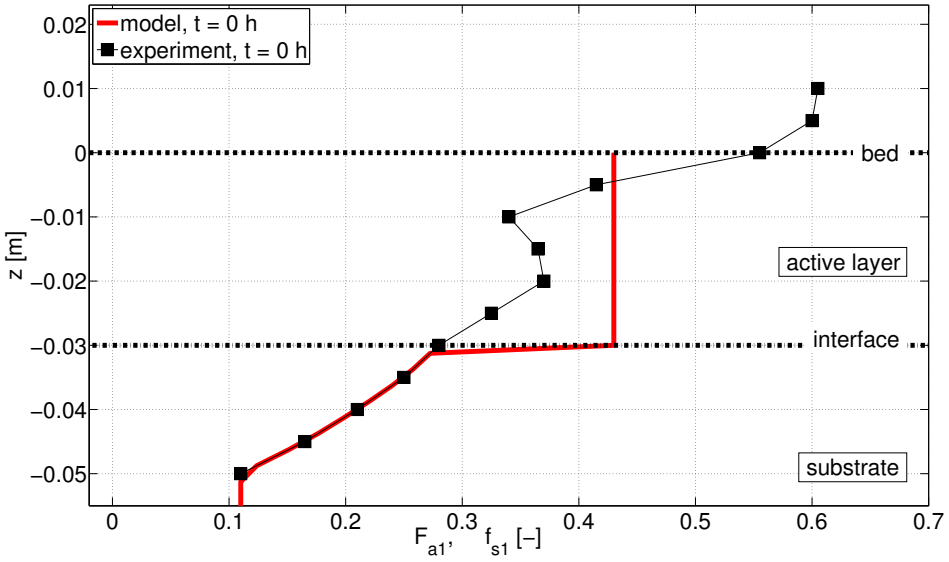

Fig. 7. Ribberink's test E8-E9. Vertical sorting profile in the experimental data and model setup at initial time $t = 0$ at the downstream end of the flume ($x = 30\,m$). Data are replotted from Ribberink [46]

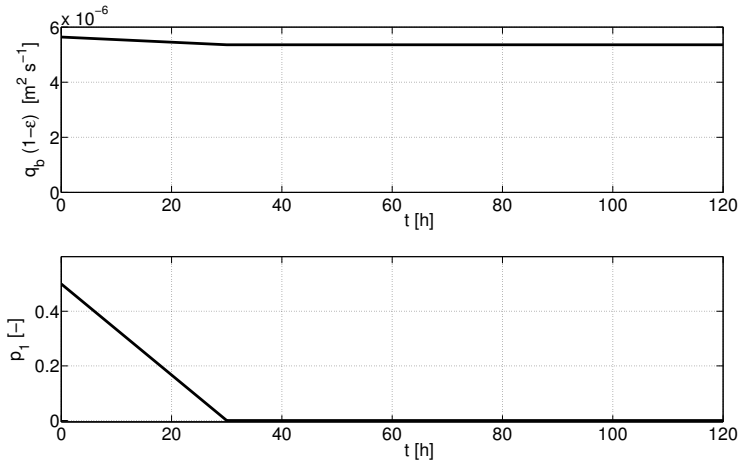

Fig. 8. Ribberink's test E8-E9. Sediment feed at the upstream boundary as function of time: total sediment discharge $q_b\,(1-\epsilon)$ and volumetric fraction content of the fine fraction in the supplied material $p_1 = q_{b1}/q_b$. Data are replotted from [46,3]

in Fig. 8, in terms of total bedload discharge and fraction content of the fine sediment in the supplied material $p_1 = q_{b1}/q_b$, as replotted from [46,3]. Initially, the total feed rate of $5.64 \cdot 10^{-6}\ m^2 s^{-1}$ was in equilibrium with transport capacity in the flume. Over the first thirty hours, the supply of fine sediment p_1 was linearly reduced from 0.5 towards 0. Meanwhile, the total sediment supply slightly reduced by about 5% due to a technical problem. Eventually, only coarse sediment was fed to the flume.

We model this case employing the second-order ADER-ENO DOT scheme, with $CFL = 0.9$ in (25). The computational domain, in the range $[0, 30]\,m$, is

discretised with 100 cells. For the calibration of friction, sediment transport and active layer thickness we rely on the previous experience in [46,3]. Friction is computed by the Chèzy law (12) with $C = 9.227$. Bedload transport is evaluated by a Meyer-Peter and Müller-type calibrated formula (14) with $A = 15.85$, $B = 1.5$, $\theta_c = 0.0307$, $\epsilon = 0.4$, and considering the hiding correction (16). In (15) we empirically calibrate a constant ripple factor $\mu = 0.315$ (value not given explicitly in [46]) for which the imposed feed at $t = 0$ matches the transport capacity in the flume (equilibrium conditions). We set the active layer thickness L_a equal to the representative dune height, for which we take a constant value of $3\,cm$, which is shown in [3] to give the best temporal match with data in the development of streamwise changes.

We discretise the substrate in sublayers of default thickness $L_s^{\text{default}} = 2.5\,mm$, which sets the numerical resolution twice as detailed as the resolution in the data. The initial vertical sorting profile imposed in the model is shown by the red thick line in Fig. 7. It can be noticed that the maximum elevation in experimental data exceeds the bed elevation computed by the model. This happens since laboratory data are affected by the local variability of bed elevation due to bedforms, whereas the numerical model only considers the average bed elevation and does not include local variations. In the active layer, only one value of F_{a1} is allowed by the Hirano model, and thus the vertical variability in the data cannot be reproduced. Here we assume $F_{a1} = 0.43$, as in [46]. This value resulted from three sampling runs through a weighted averaging procedure, taking into account the relative exposure to the flow of upper and lower portions of the dunes. In the substrate, we set the vertical sorting profile $f_{s1}(t = 0, z)$ so as to reproduce the downward coarsening trend seen in the data, and assign it as initial condition throughout the domain.

The available experimental results include time series of grainsize distribution in the active layer and bed elevation at fixed locations, streamwise profiles of grainsize distribution of the active layer at different times, time series of bedload measured at the downstream end, and the final vertical sorting profile at the downstream end. For detail on the sampling methods we refer the reader to [46,3].

Data show the time adaptation of profiles in bed elevation and grainsize distribution of the bed surface. Initially, because of the imposed increase in coarse sediment fed to the flume, the active part of the bed started to coarsen at the upstream end, and a coarsening wave progressively migrated in the downstream direction. This was accompanied by a degradational trend in bed elevation, which can be explained by the negative gradient in total bedload associated to the downstream-travelling coarsening signal [46,3]. Eventually, the bed slope adjusted to a higher value to allow the coarser material to be transported, and thus an aggradational wave propagated downstream. At $t = 120\,h$, local perturbations had moved out of the flume and a new equilibrium state

had been achieved.

4.3.2 Propagation of streamwise sorting and bed elevation changes in time

In Fig. 9 we show the time development of the grainsize distribution in the active layer, by plotting experimental and numerical series of the geometric mean diameter at three locations ($x = 4m$, $x = 14m$, $x = 24m$). Experimental and numerical data are depicted by dots and full lines, respectively. At each location, a general coarsening trend in time (i.e., a trend of increasing diameter) is detected, both in the experimental data and numerical results. Comparing the three time series, a time lag in the development of the coarsening signal is found for increasing x. This indicates the advancement of a coarsening front over the bed surface, which originates from the coarsened sediment feed at the upstream end and propagates along the flume.

At $x = 14m$ and $x = 24m$, in the first stages of the flume experiment ($t \leq 20h$), before the main visible coarsening trend takes place, experimental data show a slight decrease in the geometric mean diameter. This indicates a temporary increase in the amount of the fine fraction the bed samples with respect to the initial bed setup in these early stages. The physical reason for this process is not yet fully understood. Several possible explanations are reported in [46,3], including (i) the temporary reduction in dune height between 5 and 10 hours, which caused the vertically-averaged composition of the active bed, to be based on the upper, relatively fine, part of the bed, (ii) statistical inaccuracy due to an insufficient number of bed samples, and (iii) a fining wave, preceding the coarsening wave, due to the increased mobility of fines when the bed coarsens. The model is not able to reproduce this feature due to missing description of these physical processes. Analogous behaviour was already found even for more refined continuity models in [3].

In addition to these explanations, we propose here a fourth one, which is not based on any missing physics in the model, but on a possible mismatch between the boundary condition on sediment feed reported in [46] (see Fig. 8) and the actual experimental conditions. The initially increased content of fines might be explained by the the way the sediment feed was applied, most likely injecting sediment into the flow from above the water surface, upstream of the study reach. This may have induced the fine particles to get to the upstream end of the study reach faster than the coarse ones. If this was the case, the actual boundary condition shall include an initial phase of moderate fining, i.e. an increase in the p_1 value with respect to 0.5, which is not seen in Fig. 8, and only then the coarsening phase.

Apart from this minor mismatch, the numerical trends show fairly good agreement with the experimental ones. Over the three locations, the model well

captures the extent and time development of the coarsening trend, and the speed of the coarsening process is just slightly over-predicted at $x = 24\ m$. This confirms the validity of the assumed active layer thickness (L_a equal to the full dune height), and that the numerical solution is sufficiently able to control numerical diffusion.

Fig. 10 presents the time development of bed elevation changes at three locations ($x = 5\ m$, $x = 15\ m$, $x = 25\ m$), by experimental and numerical results. At any location we first observe a trend of bed degradation. The initial bed degradation is more clearly seen in the numerical results than in experimental data due to its small extent, but it also becomes evident in the experimental data at $x = 25m$. Comparing the three time series, the propagation of a degradational wave along the flume is observed. It is also seen that the amplitude of this wave increases in time. At each location, after the initial degradation phase, the bed aggrades, and finally reaches an almost steady configuration, characterised by higher bed elevation with respect to the initial state.

The model results well match the data at any x, thus capturing the initial phase of modest bed degradation and the subsequent aggradational phase. Unfortunately, the experimental data in Fig. 10 are available at different locations from those in Fig. 9, which does not allow for direct quantitative comparison between the two. However, it can still be discerned that for each location, the initial stage of the coarsening process is accompanied by bed degradation, both in the experimental and model results. In conclusion, Figs. 9 and 10 prove the ability of our solution to the active layer model in capturing the time development and extent of morphodynamic processes connected to streamwise sorting in this experiment.

4.3.3 Profiles of grainsize distribution in the active layer

In Fig. 11 we plot the experimental and numerical profiles of grainsize distribution in the active layer at different times ($t = 5\ h$, $t = 10\ h$, $t = 15\ h$, $t = 20\ h$, $t = 30\ h$, $t = 40\ h$). The grainsize distribution is indicated by the volumetric fraction content of the fine fraction F_{a1} as function of the streamwise coordinate x. Experimental results (reported by dotted lines) show a downstream-fining trend, which results from the imposed coarse feed and the progressive migration of the fed material along the reach. Over time, the bed surface becomes coarser close to the upstream end of the flume, and this disturbance affects a progressively extended portion of the flume. In the initial stages of the experiment ($t \leq 20\ h$), experimental data also indicate some moderate fining of the mixture found close to the bed surface with respect to the initial condition. This has already been observed in Fig. 9, and is not reproduced by our model, or by any other one in [3].

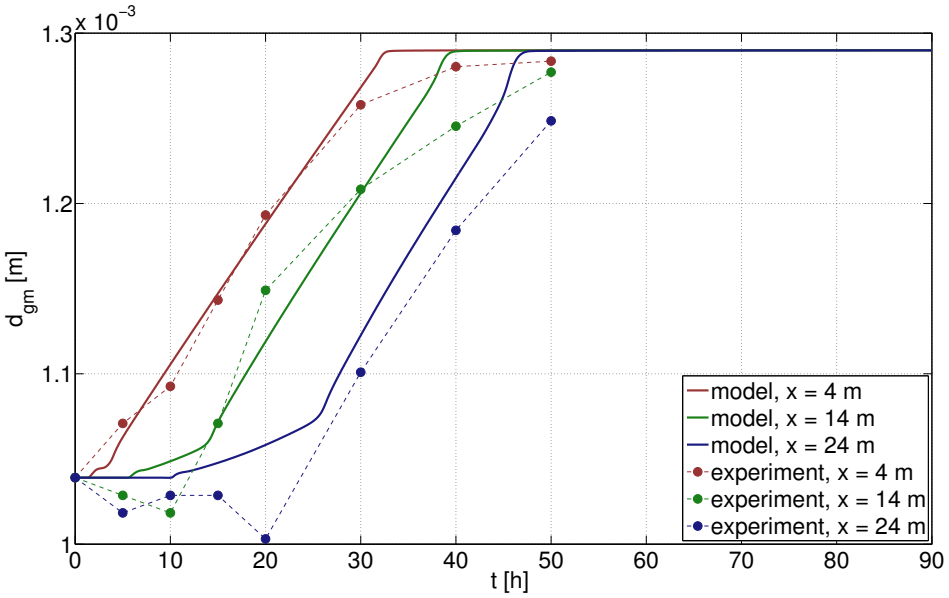

Fig. 9. Ribberink's test E8-E9. Time series of experimental data and model results of the geometric mean diameter in the active layer, at three locations ($x = 4\,m$, $x = 14\,m$, $x = 24\,m$). The numerical solution employs the ADER-ENO DOT method.

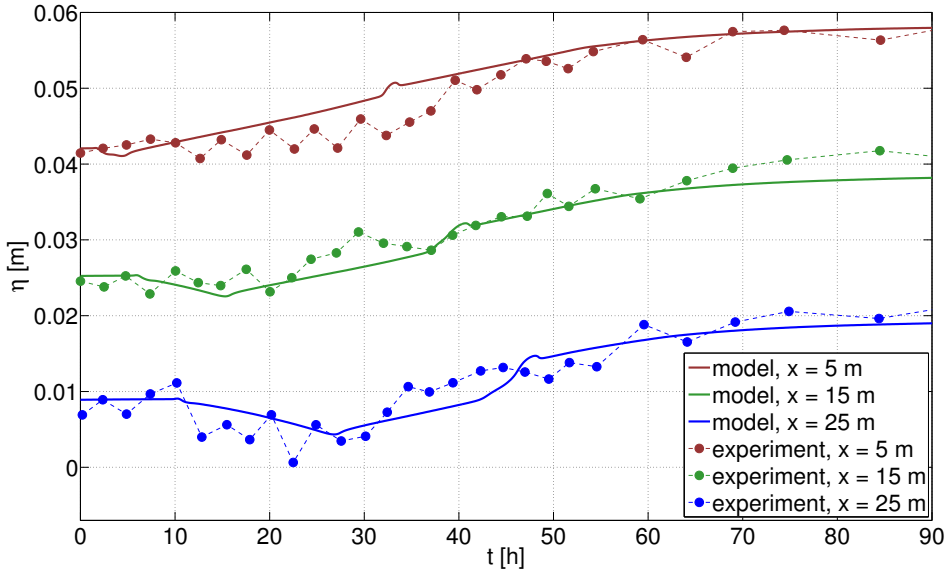

Fig. 10. Ribberink's test E8-E9. Time series of experimental data and model results of bed elevation, at three locations ($x = 5\,m$, $x = 15\,m$, $x = 25\,m$). The numerical solution employs the ADER-ENO DOT method.

Apart from this missing feature, the numerical solution provides fairly good agreement with the data. In detail, over the first 30 hours, the propagation speed of the coarsening signal is very well predicted, except for slight over-estimation at $t = 10\,h$. The numerical solution for $t \leq 20\,h$ clearly shows a knickpoint (abrupt change in slope) in the profiles of F_{a1}, which is located

at $x \sim 5.5\,m$, $x \sim 10.5\,m$, $x \sim 15\,m$, $x \sim 19.5\,m$ for $t = 5\,h$, $t = 10\,h$, $t = 15\,h$, $t = 20\,h$, respectively. Upstream of the knickpoint, the spatial sorting profiles show a marked trend of downstream fining, whereas, downstream of it, the content of the fine fraction is almost constant in space. An abrupt change in the slope of sorting profiles can also be seen in the experimental data, especially at $t = 5\,h$. Noteworthy, this behaviour had not been revealed in the previous solutions of any mixed-sediment model in [3][Figure 8], which all gave much smoother trends of downstream fining. Our solution improves the agreement with the experimental data, with respect to the solution of the Hirano model in [3][Figure 8a], for $t \leq 20\,h$, due to increased accuracy, and confirms that the active layer model is quite capable of describing streamwise sorting processes over relatively short time scales.

A mismatch is instead found at $t = 40h$ (black lines in Fig. 11), when the portion of the bed which has fully coarsened is significantly more extended in the model prediction than in the data. This has to do with the fact that the active layer concept over-simplifies the mechanics of vertical sorting within dunes. In reality, fine material is likely to be temporarily stored at relatively deep bed elevations, which are exposed to flow less frequently. Therefore, fine sediment is available for entrainment by the flow over longer time, which slows down the process of streamwise coarsening. In fact, Blom [3][Figures 8b and 8d] shows that continuity models with more detailed description of vertical sorting (Ribberink's two-layer model [46] and the SEM model with irregular bedforms [6]) correctly detect the time frame of the coarsening process in the long term.

4.3.4 Streamwise sorting and linearised solution

In our numerical solution in Fig. 11, the average speed of the knickpoint in sorting profiles is $\sim 1\,m/h$, and slightly higher in the first stages. This speed is very close to the "sorting" celerity in [46], predicted by

$$\lambda_s = \frac{q_b}{L_a} \tag{60}$$

which returns the value $\lambda_s = 1.12\,m/h$ if q_b is set equal to the value imposed at the upstream boundary. Therefore, the knickpoint quite faithfully indicates the displacement of the only "sorting" wave of the linear analysis [54], which travels at speed approximately given by (60) when a bimodal mixture is used. The predictions of the linearised theory thus have some validity even in the present real-world case characterised by very slow adjustment of flow and sediment transport, and help to interpret the laboratory data.

To carry out a comparison, in Fig. 12 we plot the numerical profiles of bed elevation at $t = 5\,h$, $t = 10\,h$, $t = 15\,h$ and $t = 20\,h$. Here, for clarity, profiles

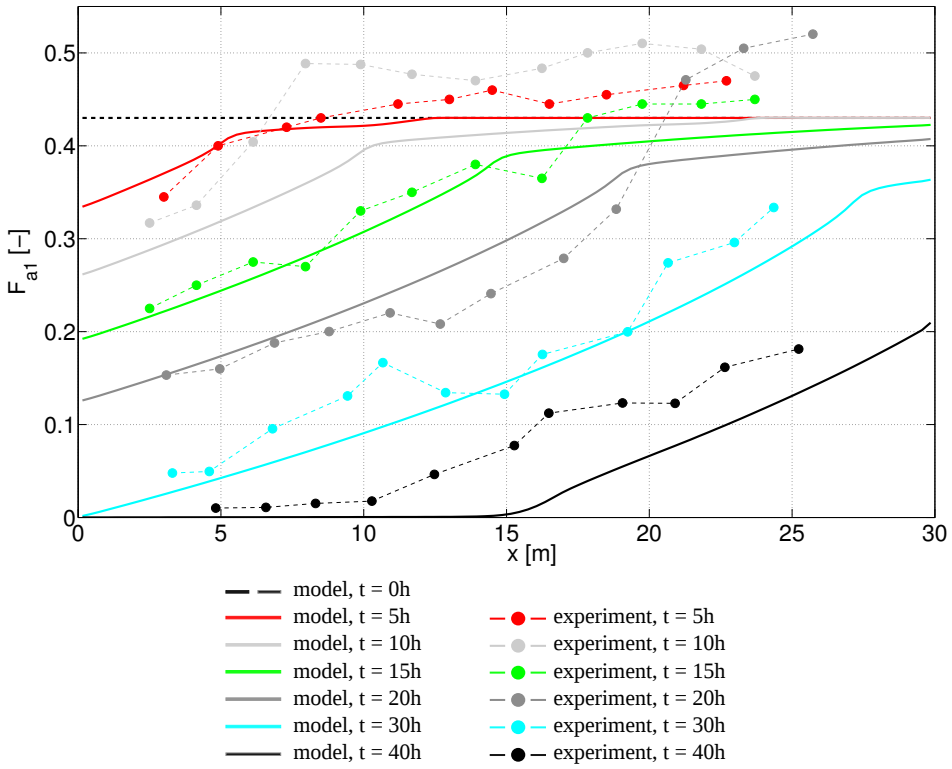

Fig. 11. Ribberink's test E8-E9. Experimental and numerical model profiles of the volume fraction content of the fine size fraction in the active layer at different times. The numerical solution employs the ADER-ENO DOT method.

have been de-trended by subtracting the initial bed $\eta\,(t = 0)$. All these bed profiles show an intermediate reach affected by bed degradation with respect to the initial condition. This reach migrates in the downstream direction in time while elongating. Amplification of the degradational signal in time is also observed.

Comparing these bed profiles with the model profiles of grainsize distribution in the active layer at the same times in Fig. 11, we notice that the degradational wave travels together with the sorting wave indicated by the knickpoint in F_{a1}, and that the minimum of each bed profile is roughly located in correspondence to the knickpoint at any time. The negative bedload gradient caused by marked streamwise fining in correspondence to the knickpoint is thus responsible for the creation of the degradational wave. This could have been foreseen simply by the linear analysis, according to which a localised streamwise increase in the amount of fine sediment in the grainsize distribution of the active layer is able to trigger associated bed degradation [54].

However, a significant deviation from the outcome of the linear analysis is given by the progressive amplification of the degradational wave. The degradational wave is seen in this exercise to amplify throughout the experiment, until it is eliminated by exiting the domain given by the flume length. This is due to

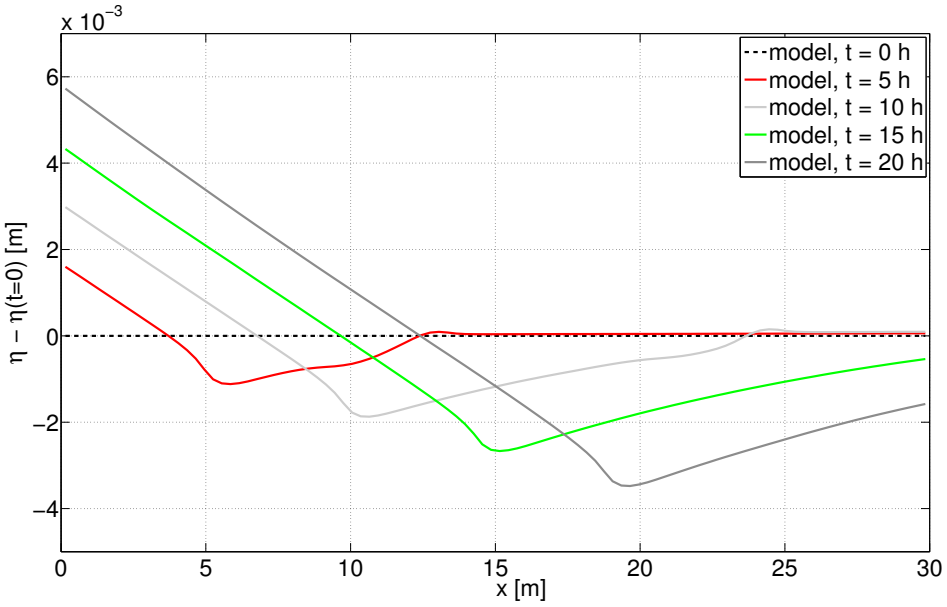

Fig. 12. Ribberink's test E8-E9: profiles of bed elevation η computed by the numerical model at different times. Profiles are de-trended by subtracting the initial bed profile $\eta\,(t=0)$. The numerical solution employs the ADER-ENO DOT method.

the fact that, in the present case, the imposed perturbation in the grainsize distribution creates a persisting negative bedload gradient in correspondence to minimum bed elevation, having finite amplitude, which travels adjoint to the knickpoint in F_{a1}.

4.3.5 Sediment transport at the downstream end

Fig. 13 reports the time evolution of bedload measured at the downstream end of the flume ($x = 30\,m$). The time series of total bedload and its grainsize distribution, indicated by the volumetric fraction content of the fine fraction $p_1 = q_{b1}/q_b$, are shown in Fig. 13a and 13b, respectively. Experimental data (dots) and numerical results (full green line) are compared, and for reference the sediment feed at the upstream end (dashed black line), already shown in Fig. 8, is reported.

Three evolution phases in Fig. 13 can be discerned. Over the first 12 hours, total bedload in Fig. 13a remains constant, as the perturbations in the grainsize distribution of the bed surface and bed elevation, described in the previous sections, have not yet reached the downstream end. This is confirmed in Fig. 13b, where the content of the fine fraction in bedload remains constant over the first 12 hours. Eventually, when the coarsening of the bed surface takes place, sediment transport in Fig. 13a starts decreasing, and the content of the fine fraction in bedload in Fig. 13b starts dropping, first at low pace, and then, after about 32 hours, at much faster pace. This trend is clearly seen in

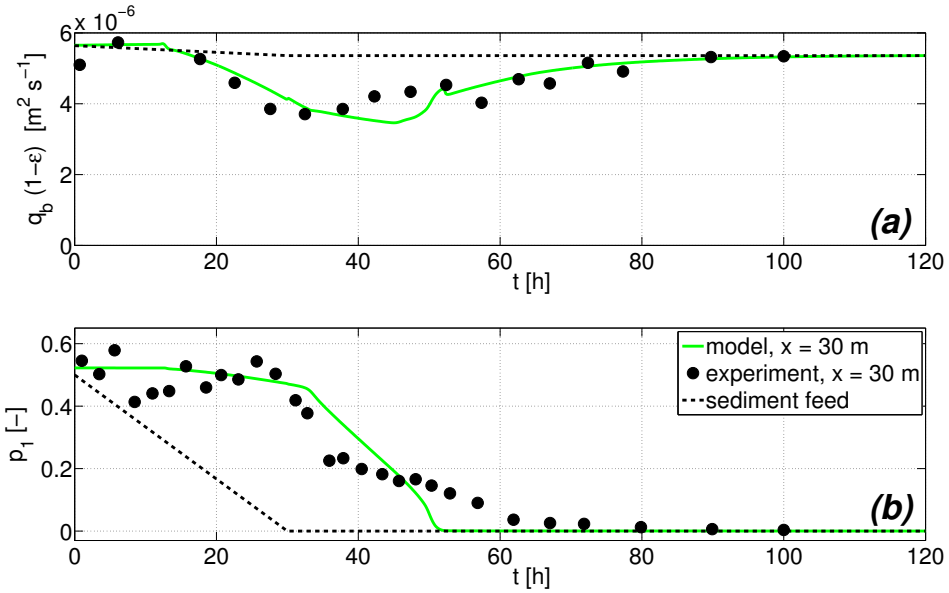

Fig. 13. Ribberink's test E8-E9. Total bedload and its grainsize distribution at the downstream end of the flume: experimental and model time series. The total sediment feed imposed at the upstream end and its grainsize distribution are also reported. The numerical solution employs the ADER-ENO DOT method.

the numerical results and confirmed by the experimental data. The complete coarsening of sediment transport in Fig. 13b is achieved after about 55 hours according to the numerical results, whereas it takes much more time (about 80 hours) in the laboratory data. In the meantime, the bed progressively increases its slope to transport the coarse bed material in equilibrium with the imposed feed, and the total sediment transport in Fig. 13a increases once again. Finally, at $t = 100\,h$, this process is completed and new equilibrium is achieved.

The model is able to reproduce the experimental trends fairly well, which demonstrates that the streamwise propagation speed of morphodynamic perturbations reaching the downstream end is reasonably well captured. However, the anticipated end of the coarsening process predicted by the model is another symptom of the excessively simplified description of vertical sorting fluxes in the active layer model, or, more precisely, its lacking description of vertical sorting fluxes. Only more refined models for mass conservation of size fractions are able to capture sorting fluxes that arise from dune migration and avalanching of particles over the bedform lee face [3]. Such more refined models account for the typical upward fining that is found in bedforms and the temporary storage of particles at relatively low elevations of the bed, that are reached by the deep bedform troughs only. These models therefore show an improved prediction of the temporal change of the grain size distribution of the load that cannot be captured with the active layer model [3].

4.3.6 Evolution of the vertical sorting profile

In Fig. 14 we plot the vertical sorting profile at the downstream end of the flume at final time ($t = 120\,h$), indicated by the fraction content of the fine fraction in the substrate f_{s1} and in the active layer F_{a1}, as function of the vertical coordinate z. As for the vertical sorting profile at initial time, presented in Fig. 7, maximum bed elevation observed in the experiment exceeds the bed elevation computed by the model, since only the experimental data include the local variability due to dunes. Nonetheless, a trend of aggradation by about $1\,cm$ over the full experiment can be found both in the experimental data and numerical results, which is in agreement with the aggradational trends already shown in Fig. 10.

Experimental data in Fig. 14 show that the active part of the bed has significantly coarsened during the experiment. The model profile in the active layer well reproduces this result. Yet, in the model the active layer has completely coarsened, whereas in the experiment it retains a small amount of fines. At lower elevations, instead, the experimental and numerical profiles in the substrate visibly differ. The experimental profile at final time presents a downward-fining behaviour until $z = -0.05\,m$, which has been significantly modified from the initial downward coarsening observed in Fig. 7. This indicates that, in the flume experiment, the grainsize distribution of the bed has been reworked quite in depth by the sorting processes occurring within bedforms. The numerical profile at final time in Fig. 14, instead, differs from the initial one only down to $z = -0.035\,m$, which is the lowest elevation reached by the active layer during the first degradational phase, and is unaltered below such elevation.

Underestimation of the vertical extent of changes in the sorting profile is once again explained by over-simplification of vertical fluxes in the active layer model. Noteworthy, this shortcoming cannot be solved by increasing the active layer thickness, since longitudinal sorting processes would be significantly slowed down, and the fairly good agreement of experimental and model results, observed in Figs. 9, 10, 11 and 13a, would be spoiled. Thus, the observed mismatch, together with those pointed out in Figs. 11 and 13b, emphasizes the limitations of the active layer approach in describing vertical sorting when the bed is covered by dunes, and points out the need for more sophisticated models of vertical sorting, see e.g. [5,3,6], for capturing these small-scale variations due to bedforms.

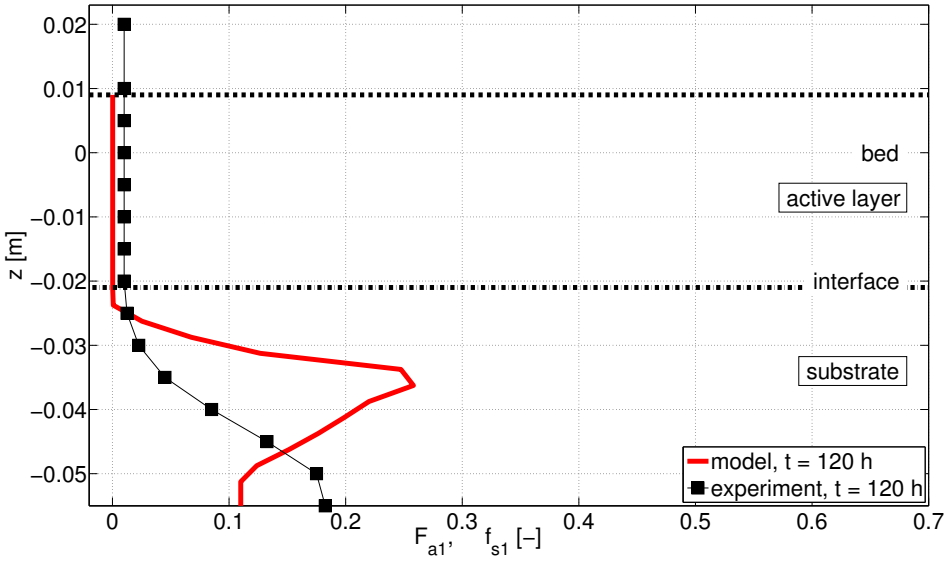

Fig. 14. Ribberink's test E8-E9. Vertical sorting profile at final time ($t = 120\,h$) of the flume experiment and numerical model. The fraction content of the fine fraction (F_{a1}, f_{s1}) is presented. The numerical solution employs the ADER-ENO DOT method.

4.3.7 Comparison of numerical schemes: streamwise sorting and bed elevation changes

In this last section we will compare the accurate solution of the DOT scheme, previously described in detail, with the solution of the PRICE-C scheme. Taking the solution of DOT as reference, we aim at investigating to what extent the physical features of the solution can still be reproduced by the cheaper and simpler PRICE-C method. The results of PRICE-C, obtained using the same mesh and setup of parameters and data as for those of DOT in the previous sections, are presented in Figs. 15 and 16.

Fig. 15 reports the streamwise profiles of the volume fraction content of the fine fraction in the active layer at different times. These profiles are visibly affected by higher spurious diffusion than those of the DOT scheme shown in Fig. 11, as they look much smoother and more smeared. Therefore, although the presence of spatial downstream-coarsening trends and the progressive coarsening of increasing portions of the domain are still observed in the solution of PRICE-C, the knickpoints previously observed in the profiles of DOT at $t \leq 20\,h$ are not detectable here. It is thus impossible here to estimate the speed of the "sorting" wave based on the present solution, as previously done for the solution of DOT. Noteworthy, spurious diffusion has a major impact also on the profiles at $t \geq 30\,h$. In detail, at $t \geq 40\,h$, when the active layer shall have entirely coarsened until $x \sim 15\,m$ according to the solution of DOT (Fig. 11), the solution of PRICE still predicts the presence of a significant amount of fines throughout the domain, except close to the upstream boundary. This can

be explained by observing that (numerical) diffusion is a symmetrical process, and thus a diffusive solution is also likely to predict an upstream-propagating "sorting" effect, rather than a purely downstream-propagating one as foreseen by the linear analysis of the hyperbolic system [46,54] and by the solution of DOT.

In conclusion, the propagation of streamwise sorting processes here appears to be controlled by numerical diffusion rather than linked to the characteristic speed of the linearised theory, which has three major drawbacks. First, the general agreement between the present solution and the experimental data is poorer than in the case of the solution of DOT. Second, the calibration of parameters controlling the "sorting speed" (essentially, the active layer thickness L_a) cannot be precisely assessed against the data, since the numerically computed propagation speed significantly differs from the theoretical one, and even the propagation direction of streamwise sorting is altered by the presence of diffusion. Third, unlike we did in Section 4.3.3 with reference to the solution of DOT at $40\,h$, it is hard to discern whether the observed mismatch with the experimental profiles are only due to numerical inaccuracy, or are the symptom of over-simplified representation of the physics.

The impact of such inaccurate representation of streamwise sorting on the evolution of the bed profile shall finally be investigated. In Fig. 16 we report the time development of bed elevation computed by the PRICE-C scheme. We observe that the initial degradational phase associated to the propagation of a "sorting" wave is here essentially neglected, unlike in the solution of DOT in Fig. 10. This behaviour is a consequence of the excessively mild sorting profiles observed in Fig. 15, where the relatively sharp gradients of total bedload needed to produce local bed degradation have been smoothed out. This comparison thus emphasizes the need of accurate numerical solutions to capture the physical processes which are predicted by the underlying equations, and to challenge the validity of the adopted physical schematisation.

5 Conclusions

We have presented a novel numerical solution of the one-dimensional Saint-Venant-Hirano model for mixed-sediment morphodynamics, based on the recently introduced matrix-vector formulation of the system [54]. The resulting fully-unsteady, non-conservative system of PDEs, which is hyperbolic for the range of data used in the applications of this paper, is solved using a path-conservative technique in the Finite Volume framework, which is embedded in a splitting procedure for the treatment of frictional source terms. The solution procedure employs the DOT upwind scheme, extended to second-order accuracy in space and time using the ADER-ENO technique. The model in-

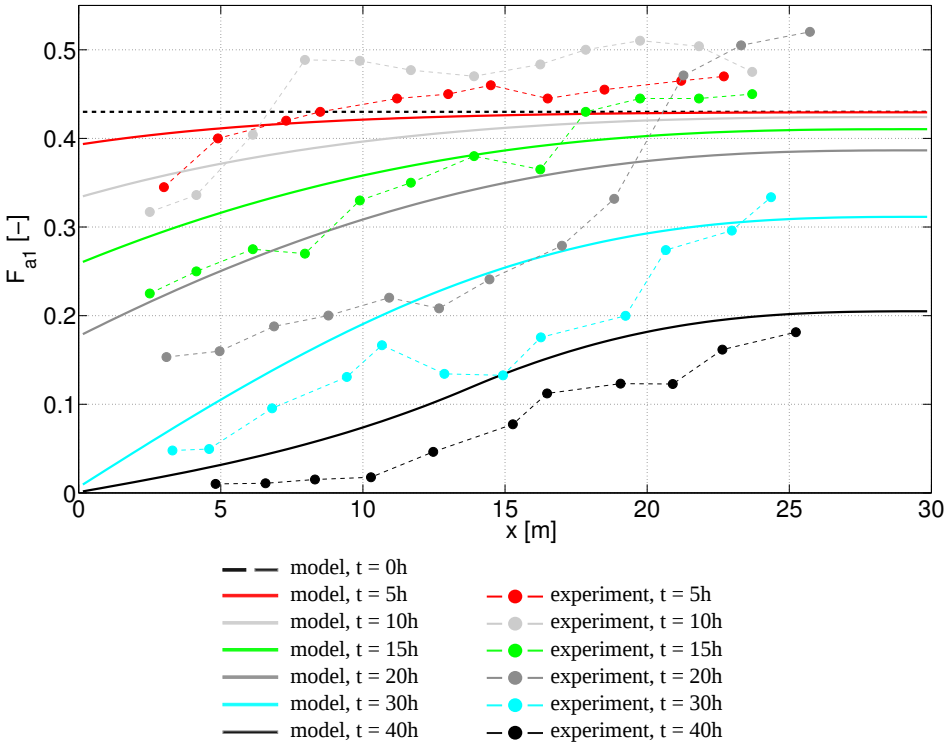

Fig. 15. Ribberink's test E8-E9. Experimental and numerical model profiles of the volume fraction content of the fine size fraction in the active layer at different times. The numerical solution employs the ADER-ENO PRICE-C method.

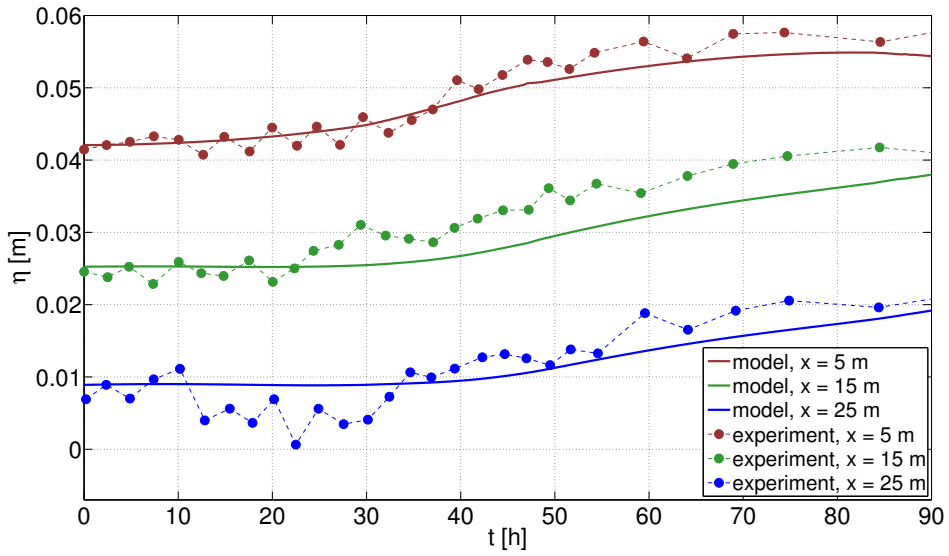

Fig. 16. Ribberink's test E8-E9. Time series of experimental data and model results of bed elevation, at three locations ($x = 5\,m$, $x = 15\,m$, $x = 25\,m$). The numerical solution employs the ADER-ENO PRICE-C method.

cludes a mass-conservative procedure for bookkeeping of size stratification in the substrate, suitable for our Finite Volume technique.

We have introduced a concept of balancedness which applies to the vertical sediment flux from the substrate to the active layer under degradational conditions, preventing the alteration of the grainsize distribution of the substrate in this case, and we have suitably modified the DOT scheme to satisfy this balancedness requirement.

Finally, we have assessed the model using three numerical applications. First, in a test case conducted under conditions of bed degradation and armouring due to lack of sediment supply, we have experimentally shown the importance of using a balanced scheme in practical cases. Then, in the second test, we have evaluated the model performance in addressing the propagation of small-amplitude hydro-morphodynamic waves triggered by an initial imbalance in the grainsize distribution in the active layer. This case, here proposed for the first time, has an analytical solution, which enables us to prove the convergence of our numerical solution and assess its accuracy using a fully-mathematical benchmark. Last, we have numerically reproduced Ribberink's laboratory experiment E8-E9, which includes streamwise and vertical sorting and changes in the bed elevation profile. Our numerical solution improves the presently available modelling reproductions of this setup with respect streamwise morphodynamic processes, and enables us to analyse the propagation speed of morphodynamic changes by comparison with linearised theories. However, the proposed solution is still limited by the simplifications of the underlying active layer approach in describing vertical sorting within bedforms, and discrepancies with the data arise especially in the description of the evolution of size stratification.

A Quasi-conservative formulation and numerical schemes

We present here the quasi-conservative counterpart to the non-conservative formulation (17), and show how this can be employed to derive alternative numerical solutions in the path-conservative framework.

The quasi-conservative formulation of the Saint-Venant-Hirano model reads

$$\partial_t \mathbf{Q} + \partial_x \mathbf{F}\left(\mathbf{Q}\right) + \mathbf{B}\partial_x \mathbf{Q} = \mathbf{S}\ , \tag{A.1}$$

where vectors $\mathbf{Q}$ and $\mathbf{S}$ have been defined in (18) and (19) respectively, and

the flux vector $\mathbf{F}(\mathbf{Q})$ and the matrix $\mathbf{B}$ are given by

$$\mathbf{F}(\mathbf{Q}) = \begin{bmatrix} q + q_b \\ u^2 h + \frac{1}{2} g h \\ q_b \\ \hline q_{bk} - f_k^I q_b \\ \hline f_k^I q_b \end{bmatrix} \begin{matrix} \}1 \\ \}1 \\ \}1 \\ \}N-1 \\ \}N-1 \end{matrix} \quad , \quad \mathbf{B} = \left[\begin{array}{ccc|cc} 0 & 0 & 0 & 0 & 0 \\ 0 & 0 & gh & 0 & 0 \\ 0 & 0 & 0 & 0 & 0 \\ \hline 0 & 0 & 0 & 0 & 0 \\ \hline \underbrace{0}_{1} & \underbrace{0}_{1} & \underbrace{0}_{1} & \underbrace{0}_{N-1} & \underbrace{0}_{N-1} \end{array}\right] \begin{matrix} \}1 \\ \}1 \\ \}1 \\ \}N-1 \\ \}N-1 \end{matrix} \quad . \tag{A.2}$$

With the adoption of a quasi-conservative formulation like (A.1), the first-order scheme (26) of the DOT type can be recast as

$$\mathbf{D}^{\pm}_{i+\frac{1}{2}} = \frac{1}{2} \left\{ \mathbf{F}\left(\overline{\mathbf{Q}}_{i+1}\right) - \mathbf{F}\left(\overline{\mathbf{Q}}_i\right) + \hat{\mathbf{B}}_{i+\frac{1}{2}} \left(\overline{\mathbf{Q}}_{i+1} - \overline{\mathbf{Q}}_i\right) \pm \left|\hat{\mathbf{A}}_{i+\frac{1}{2}}\right| \left(\overline{\mathbf{Q}}_{i+1} - \overline{\mathbf{Q}}_i\right) \right\} , \tag{A.3}$$

where, under the assumption of a segment path (28), $\left|\hat{\mathbf{A}}_{i+\frac{1}{2}}\right|$ is given by (31) and (32), and $\hat{\mathbf{B}}_{i+\frac{1}{2}}$ is analogously defined as

$$\hat{\mathbf{B}}_{i+\frac{1}{2}} = \int_0^1 \mathbf{B}\left(\mathbf{\Psi}\left(\overline{\mathbf{Q}}_i, \overline{\mathbf{Q}}_{i+1}, s\right)\right) \mathrm{d}s \, . \tag{A.4}$$

We notice that for the case at hand $\hat{\mathbf{B}}_{i+\frac{1}{2}}$ can be easily integrated analytically in exact manner. Anyway, this does not diminish the computational overhead of the method, which is connected to the calculation of $\left|\hat{\mathbf{A}}_{i+\frac{1}{2}}\right|$.

With exact $\hat{\mathbf{B}}_{i+\frac{1}{2}}$, the advantage of the formulation (A.1) over (27) is that the consistency property of the method is not influenced by accuracy in the quadrature rule, hence conservation should be maintained exactly. Before this strategy can be applied to the Saint-Venant-Hirano model, however, the issues connected to vertical mass balancedness shall be discussed again for the scheme (A.3).

Acknowledgements

The contribution of Guglielmo Stecca to this research has been funded by a Marie Curie International Outgoing Fellowship (project "BraidSideEarth", grant 2013-621886) within the 7th European Community Framework Programme, and by Aspasia scholarship 015.007.051 of the Netherlands Organization for Scientific Research (NWO).

The authors thank the editor and two anonymous reviewers for their construc-

tive remarks, which helped improving the clarity and content of this paper.

References

[1] K. Ashida and M. Michiue. An investigation of bed degradation downstream of a dam. volume 3, pages 247–255. International association of Hydrological Sciences, Wallingford, U.K., 1971. 14th Congress IAHR.

[2] A. Bermúdez and M. E. Vázquez-Cendón. Upwind methods for hyperbolic conservation laws with source terms. *Computers and Fluids*, 23(8):1049–1071, 1994.

[3] A. Blom. Different approaches to handling vertical and streamwise sorting in modeling river morphodynamics. *Water Resources Research*, 44(W03415), 2008.

[4] A. Blom and G. Parker. Vertical sorting and the morphodynamics of bedform-dominated rivers: A modeling framework. *Journal of Geophysical Research*, 109(F02007), 2004.

[5] A. Blom, J. S. Ribberink, and H. J. de Vriend. Vertical sorting in bed forms: Flume experiments with a natural and a trimodal sediment mixture. *Water Resources Research*, 39(2), 2003.

[6] A. Blom, J. S. Ribberink, and G. Parker. Vertical sorting and the morphodynamics of bed form-dominated rivers: a sorting evolution model. *Journal of Geophysical Research*, 113(F01019), 2008.

[7] A. Canestrelli, M. Dumbser, A. Siviglia, and E. Toro. Well-balanced high-order centred schemes on unstructured meshes for shallow water equations with fixed and mobile bed. *Advances in Water Resources*, 33:291–303, 2010.

[8] A. Canestrelli, A. Siviglia, M. Dumbser, and E. Toro. Well-balanced high-order centred schemes for non-conservative hyperbolic systems. Applications to shallow water equations with fixed and mobile bed. *Advances in Water Resources*, 32(6):834–844, 2009.

[9] M. J. Castro-Díaz, E. D. Fernández-Nieto, and A. M. Ferreiro. Sediment transport models in shallow water equations and numerical approach by high order finite volume methods. *Computers & Fluids*, 37(3):299–316, 2008.

[10] M. J. Castro-Díaz, E. D. Fernández-Nieto, A. M. Ferreiro, and C. Parés. Two-dimensional sediment transport models in shallow water equations. a second order finite volume approach on unstructured meshes. *Computer Methods in Applied Mechanics and Engineering*, 198(33-36):2520–2538, 2009.

[11] M. J. Castro-Díaz, E. D. Fernández-Nieto, M. J. González-Vida, and C. Parés. Numerical treatment of the loss of hyperbolicity of the two-layer shallow-water system. *Journal of Scientific Computing*, 48(1–3):16–40, 2011.

[12] M. J. Castro-Díaz, J. M. Gallardo, and A. Marquina. Approximate Osher-Solomon schemes for hyperbolic systems. 2014. Preprint submitted to Applied Mathematics and Computation.

[13] V. Chavarrías, G. Stecca, A. Siviglia, and A. Blom. Ellipticity of the Saint-Venant-Hirano model for mixed-sediment river morphodynamics. 2015. River, Coastal and Estuarine Morphodynamics (RCEM), Iquitos, Peru.

[14] V. Chavarrías, G. Stecca, E. Viparelli, and A. Blom. Ellipticity in modelling mixed sediment morphodynamics. 2014. Netherlands Centre for River studies (NCR), University of Twente, Enschede, Netherlands.

[15] V. T. Chow. *Open-channel hydraulics*. McGraw-Hill, New York, 1959. 680 p.

[16] M. Colombini and G. Parker. Longitudinal streaks. *Journal of Fluid Mechanics*, 304:161–183, 1995.

[17] S. Cordier, M. H. Le, and T. Morales de Luna. Bedload transport in shallow water models:: Why splitting (may) fail, how hyperbolicity (can) help. *Advances in Water Resources*, 34:980–989, 2011.

[18] Y. Cui, C. Paola, and G. Parker. Numerical simulation of aggradation and downstream fining. *Journal of Hydraulic Research*, 34:185–204.

[19] Y. Cui and G. Parker. Numerical model of sediment pulses and supply disturbances in mountain rivers. *ASCE Journal of Hydraulic Engineering*, 131(8):646–656, 2005.

[20] Y. Cui, G. Parker, J. Pizzuto, and T. E. Lisle. Sediment pulses in mountain streams: 2. comparison between experiments and numerical predictions. *Water Resources Research*, 39(9), 2003.

[21] G. Dal Maso, P. Le Floch, and F. Murat. Definition and weak stability of nonconservative products. *Journal de Mathematiques pures et appliques*, 74(6):483–548, 1995.

[22] M. de Vries. Considerations about non-steady bed-load transport in open channels. 1965. 11th Congress IAHR, Int. Assoc. for Hydraul. Res., Leningrad, Russia.

[23] M. Dumbser and E. F. Toro. A simple extension of the osher riemann solver to non-conservative hyperbolic systems. *Journal of Scientific Computing*, 48(1–3), 2011.

[24] V. I. Egiazaroff. Calculation of non-uniform sediment concentrations. *J. of Hydr. Div., ASCE*, 91(HY4), 1965.

[25] A. Harten, B. Engquist, S. Osher, and S. R. Chakravarthy. Uniformly high order accuracy essentially non-oscillatory schemes iii. *Journal of Computational Physics*, 71(2):231–303, 1987.

[26] M. Hirano. River bed degradation with armoring. *Transactions of the Japanese Society of Civil Engineering*, (3):194–195, 1971.

[27] M. Hirano. Studies on variation and equilibrium state of a river bed composed of nonuniform material. *Transactions of the Japanese Society of Civil Engineering*, (4):128–129, 1972.

[28] T. B. Hoey and R. I. Ferguson. Numerical simulation of downstream fining by selective transport in gravel bed rivers: Model development and illustration. *Water Resources Research*, 30:2251–2260, 1994.

[29] P. Hu, Z. Cao, G. Pender, and H. Liu. Numerical modelling of riverbed grain size stratigraphic evolution. *International Journal of Sediment Research*, 29:329–343, 2014.

[30] D. D. Joseph and J. C. Saut. Short-wave instabilities and ill-posed initial-value problems. *Theoretical and Computational Fluid Dynamics*, 1:191–227, 1990.

[31] C. Juez, J. Murillo, and P. García-Navarro. A 2D weakly-coupled and efficient numerical model for transient shallow flow and movable bed. *Advances in Water Resources*, 71:93–109, 2014.

[32] S. Lanzoni, A. Siviglia, A. Frascati, and G. Seminara. Long waves in erodible channels and morphodynamic influence. *Water Resources Research*, 42(W06D17), 2006. W06D17, doi:10.1029/2006WR004916.

[33] S. Lanzoni and M. Tubino. Grain sorting and bar instability. *Journal of Fluid Mechanics*, 393:149–174, 1999.

[34] D. A. Lyn. Unsteady sediment transport modeling. *Journal of Hydraulic Engineering, ASCE*, 113(1):1–15, 1987.

[35] D. A. Lyn and M. Altinakar. St. Venant Exner equations for near-critical and transcritical flows. *Journal of Hydraulic Engineering, ASCE*, 128(6):579–587, 2002.

[36] G. A. Mazza de Almeida and J. F. Rodríguez. Understanding pool-riffle dynamics through continuous morphological simulations. *Water Resources Research*, 47(W01502), 2011.

[37] E. Meyer-Peter and R. Müller. Formulas for bedload transport. In *2nd Meeting, Int. Assoc. of Hydraul. Eng. and Res.* Stockholm, 1948.

[38] E. Mosselman. Modelling sediment transport and morphodynamics of gravel-bed rivers. In *Gravel bed rivers: processes, tools, environments*, pages 101–115. Wiley and Sons Ltd, 2012.

[39] E. Mosselman, K. Sloff, and S. van Vuren. Different sediment mixtures at constant flow conditions can produce the same celerity of bed disturbances. pages 1373–1377, 2008. River Flow 2008, Proceedings of the International Conference on Fluvial Hydraulics.

[40] S. Osher and F. Solomon. Upwind difference schemes for hyperbolic conservation laws. *Mathematics of Computation*, 38:339–374, 1982.

[41] C. Parés. Numerical methods for non-conservative hyperbolic systems: a theoretical framework. *SIAM Journal of Numerical Analysis*, 44:300–321, 2006.

[42] G. Parker. *E-book on 1D sediment transport morphodynamics with applications to rivers and turbidity currents [online].*

[43] G. Parker. Selective sorting and abrasion of river gravel. I. theory. *ASCE Journal of Hydraulic Engineering*, 117:113–149, 1991.

[44] G. Parker and E. D. Andrews. Sorting of bed load sediment by flow in meander bends. *Water Resources Research*, 21(9):1361–1373, 1985.

[45] G. Parker, C. Paola, and S. Leclair. Probabilistic exner sediment continuity equation for mixtures with no active layer. *ASCE Journal of Hydraulic Engineering*, 126:818–826, 2000.

[46] J. S. Ribberink. *Mathematical modelling of one-dimensional morphological changes in rivers with non-uniform sediment*. PhD thesis, Delft University of Technology, Delft, Netherlands, 1987. http://repository.tudelft.nl/view/ir/uuid%3Abdfc1519-a71d-4752-83f7-3ebf1bb890e9/.

[47] G. Seminara, M. Colombini, and G. Parker. Nearly pure sorting waves and formation of bedload sheets. *Journal of Fluid Mechanics*, (312):253–278, 1996.

[48] Y. Shekari and E. Hajidavalloo. Application of Osher and PRICE-C schemes to solve compressible isothermal two-fluid models of two-phase flow. *Computers & Fluids*, 86:363–379, 2013.

[49] J. Sieben. *Modelling of hydraulics and morphology in mountain rivers*. PhD thesis, Delft University of Technology, Netherlands, 1997.

[50] A. Siviglia, G. Stecca, D. Vanzo, G. Zolezzi, E. F. Toro, and M. Tubino. Numerical modelling of two-dimensional morphodynamcs with applications to river bars and bifurcations. *Advances in Water Resources*, 53:243–260, 2013.

[51] C. J. Sloff, H. R. A. Jagers, Y. Kitamura, and P. Kitamura. 2D morphodynamic modelling with graded sediment. 2001. paper presented at the 2nd Symposium on River, Coastal and Estuarine Morphodynamics, Int. Assoc. for Hydraul. Res., Obihiro, Japan.

[52] C. J. Sloff and E. Mosselman. Bifurcation modelling in a meandering gravel-sand bed rivers. *Earth Surface Processes and Landforms*, (37):1556–1566, 2012.

[53] G. Stecca. *Numerical modelling of gravel-bed river morphodynamics*. PhD thesis, University of Trento, Italy, 2012. Available at http://eprints-phd.biblio.unitn.it/769/.

[54] G. Stecca, A. Siviglia, and A. Blom. Mathematical analysis of the Saint-Venant-Hirano model for mixed-sediment morphodynamics. *Water Resources Research*, 50(10):7563–7589, 2014.

[55] G. Stecca, A. Siviglia, and E. Toro. A finite volume upwind-biased centred scheme for hyperbolic systems of conservation laws. Applications to shallow water equations. *Communications in Computational Physics*, 12(4):1183–1214, 2012.

[56] P. Tassi, S. Rhebergen, C. Vionnet, and O. Bokhove. A discontinuous Galerkin finite element model for river bed evolution under shallow flows. *Computer Methods in Applied Mechanics and Engineering*, (197):2930–2947, 2008.

[57] E. F. Toro. *Shock-Capturing Methods for Free-Surface Shallow Flows*. Wiley and Sons Ltd, 2001.

[58] E. F. Toro. *Riemann Solvers and Numerical Methods for Fluid Dynamics*. Springer–Verlag, 2009.

[59] E. F. Toro and V. A. Titarev. Solution of the generalized Riemann problem for advection-reaction equations. *Proceedings of the Royal Society of London Series A. Mathematical Physical and Engineering Sciences*, 458(2018):271–281, 2002.

[60] C. M. Toro-Escobar, G. Parker, and C. Paola. Transfer function for the deposition of poorly sorted gravel in response to streambed aggradation. *Journal of Hydraulic Research*, 34(16):35–53, 1996.

[61] D. F. Vetsch, D. Ehrbar, M. Gerber, S. Peter, P. Russelot, C. Volz, L. Vonwiller, R. Faeh, D. Farshi, R. Mueller, and R. Veprek. System manuals of BASEMENT. Software manual, VAW, ETH Zurich, 2014. v. 2.4.

[62] E. Viparelli, A. Blom, C. Ferrer-Boix, and R. Kuprenas. Comparison between experimental and numerical stratigraphy emplaced by a prograding delta. *Earth Surface Dynamics*, 2:323–338, 2014.

[63] E. Viparelli, O. E. Sequeiros, A. Cantelli, P. R. Wilcock, and G. Parker. River morphodynamics with creation/consumption of grain size stratigraphy 2: numerical model. *Journal of Hydraulic Research*, 46(6):726–741, 2010.